Effect of the transition layer on the stability of a fluid-porous configuration: Impact on power-law rheology

Sourav Sengupta and Sirshendu De*
Department of Chemical Engineering, Indian Institute of Technology Kharagpur, Kharagpur 721302, India

(Received 5 December 2020; accepted 18 May 2021; published 9 June 2021)

One of the crucial aspects in the case of describing flow through a fluid-porous double layer configuration is the quantification of the flow behavior near the fluid-porous interface. Both theoretical as well as experimental studies indicate that in the case of real-life fluid-porous geometries, the shift from the fluid layer to the porous layer is not sharp and immediate. Instead, there exists a transition layer in between the fluid and the porous layers. In order to get a realistic picture of flow transition characteristics for such systems, it is imperative that this transition layer be taken into consideration in the hydrodynamic stability analysis. The same has been carried out in the present study, and the effect of the transition layer on the stability characteristics has been assessed. The current study has investigated the effect of the transition layer on the flow of a power-law fluid overlying a porous layer in a channel flow configuration, as the earlier studies were restricted to Newtonian fluids only. A rigorous three-dimensional perturbation framework has been adopted, as Squire's theorem is not applicable for the power-law rheology unlike Newtonian rheology. Both modal and nonmodal analyses are attempted in order to reveal the long-time response as well as short-time amplifications of the system to external disturbances. The intricate interaction between the non-Newtonian rheology of the fluid and the thin transition layer is found to affect the transient amplifications of the flow system significantly.

DOI: 10.1103/PhysRevFluids.6.063902

I. INTRODUCTION

Fluid flow over a porous layer has several important applications in numerous geological, biological, and industrial circumstances [1–6]. Owing to its practical relevance, there is a large volume of studies dedicated to throwing light on various aspects of this flow situation. The earliest reported study can be traced back to the time of Darcy [7], who dealt with the flow of water over a sand bed.

Traditionally, the modeling of combined porous-fluid flows has been carried out by either one-domain or two-domain approaches [8]. In the one-domain method, there is a single equation modeling the entire flow region (both the fluid and the porous regions). On the contrary, a two-domain approach advocates the use of separate momentum equations to model the fluid and the porous zones, and the two zones are connected by a suitable condition at the interface. Both these approaches have been widely adopted by researchers to model the flow behavior.

Vafai and Tien [9] stressed the need to consider the boundary and inertia effects in convective flow and heat transfer in the case of fluid-porous systems with a constant porosity. A quantification of these effects was carried out in terms of associated governing parameters. Consequently, a fundamental characterization scheme was constituted for assessing the relevance of Darcy's law toward describing several problems of flow and heat transfer in fluid-porous systems.

*Corresponding author: sde@che.iitkgp.ac.in

A traditional yet fairly successful way to model flow in porous media is the continuum approach. In the continuum approach, it is assumed that there is a continuous spatial distribution of the pertinent characterizing properties of flow, such as pressure, temperature, velocity, etc. This macroscopic approach is particularly suited for flow in porous media, due to the computational difficulties associated with the consideration of a geometrically complex porous media at a microscopic level. Within the framework of the continuum approach, a popular methodology is the technique of volume averaging, wherein the measurable quantities are obtained by averaging over volumes [10]. In this technique, a macroscopic variable (it can be velocity, pressure, etc.) is assumed to have a value over the smallest admissible functional volume, known as the representative elementary volume (REV). It is further assumed that the REV is sufficiently large, so that there is an insignificant fluctuation of the spatially averaged properties.

The finite-volume method (FVM) is another important tool for modeling porous flows. The study by Das, Nassehi, and Wakeman [11] adopted the FVM to carry out the numerical simulation for investigating subsurface water (groundwater) flows. They highlighted the necessity of modeling flow in the combined "free" (i.e., fluid) and porous layers, instead of flow modeling in the porous domain alone. Hanspal *et al.* [12] developed a model for simulating the hydrodynamics (flow and pressure drop) of combined free and porous flows in the context of industrial (both cross-flow and dead-end) filtration processes. A power-law fluid rheology was considered for the purpose. A two-domain formulation was adopted, modeling the flow in the free (fluid) and the porous domains by the Cauchy momentum and Darcy equations, respectively. The shear-thickening fluids were shown to yield a higher pressure drop compared to the Newtonian and shear-thinning fluids.

The studies by Bruneau and Mortazavi [13,14] have advocated the use of the "penalization method" (which is essentially based on the Brinkman-Navier-Stokes equations) for modeling bluff body flows involving porous media, wherein they have adopted a Brinkman-based formulation to describe the entire fluid and porous regions. While doing so, the fluid layer is assumed to have a permeability of infinity, while a permeability of zero is considered for the solid (impermeable) region. On the other hand, the porous layer has a permeability in between zero and infinity.

However, a majority of the fluid-porous systems encountered in a practical setting involves non-Newtonian fluids [15–17]. In fact, there are two principal aspects for a proper mathematical description of the flow in fluid-porous systems. The first one is the selection of an appropriate model that quantifies the fluid rheology. Second, one needs to have a realistic mathematical description of the porous layer. In this regard, a major aspect in the case of describing flow through a fluid-porous double layer configuration is the quantification of the flow behavior near the fluid-porous interface. A number of theoretical, numerical, and experimental studies are devoted to address this critical issue [1,2]. These studies reveal that in the case of real-life fluid-porous geometries, there is no sudden shift from the fluid layer to the porous layer as predicted by the Darcy model. In reality, there exists a thin transition layer in between the fluid and the porous layers. A major advantage in the consideration of a transition layer is that it takes into account the fluid-fluid viscous interaction that becomes significant in the proximity of the fluid-porous interface. Thus, if one wishes to conduct a hydrodynamic stability analysis for such a system to comprehend the flow transition characteristics, it would not be prudent to neglect the effect of this transition layer. The same has been carried out in the present study, and the effect of the transition layer on the stability characteristics has been assessed in the context of a non-Newtonian fluid-porous system.

A power-law fluid has been considered in the present study to represent the non-Newtonian rheology. Flow of a non-Newtonian fluid over a porous layer exhibits numerous occurrences in bio-fluid dynamics, petroleum engineering, polymer processing, etc. Thus, it is crucial to gain a fundamental understanding regarding the flow transition characteristics of the same. The present study is probably the first account of hydrodynamic stability analysis of a non-Newtonian fluid-porous system involving a transition porous layer. There are reported studies in the literature dealing with the thermal convective instabilities of a power-law fluid-porous system [18,19]. However, to the best of our knowledge, no analysis of shear instability for such a configuration exists in the literature.

Additionally, it is essential to elucidate the reason for consideration of a three-layer system (i.e., a fluid layer and a porous Darcy layer with a Brinkman transition layer in between) instead of considering a two-layer (a fluid layer and a single Darcy-Brinkman layer throughout the porous media) configuration. Such a choice is attributed to the fact that the Brinkman term (i.e., the Laplacian term) is simply not valid in a location away from the fluid-porous interface, as demonstrated in several analytical and experimental studies (see Nield and Bejan [20], and references therein). In other words, the Darcy-Brinkman equation is valid only within the transition layer [21]. In the case of a horizontal channel flow of a fluid overlying a porous layer, there seems to be a long-standing debate on the applicability of various porous models (Brinkman, Darcy, Forchheimer) in describing flow through the porous layer [21–24]. The Darcy model, being the simplest of the three, has naturally been the first choice. The same has been used in the case of stability studies as well [25–32]. On the other hand, there seems to be a consensus that for a porous layer having high porosity (> 0.7), the Brinkman model is a more appropriate consideration [20,33,34]. As a result, there have been stability analyses for highly porous media (e.g., Foametal), modeling the entire porous layer by Brinkman equations [35–37]. However, for low-porosity media, the application of the Brinkman model throughout the porous layer is not suitable. In fact, Liu *et al.* [36] have observed that for a porous material having low porosity, the stability analyses yield substantially different results for Darcy and Brinkman models. For realistic description of a dense porous layer, several studies (both theoretical and experimental) have advocated the use of a porous transition layer in between the fluid and the Darcy layer [1,2,38–46]. In fact, the experimental determination of the transition layer thickness [2,40,43] has resulted in an important revelation: the depth of the transition layer (d_{TL}) is much higher than $\sqrt{K}$, where K is the permeability of the porous media (in fact, $d_{TL}/\sqrt{K} = O(50)$, as reported by Goharzadeh, Khalili, and Jorgensen [2]). This is in stark contrast to many earlier studies estimating $d_{TL}/\sqrt{K} = O(1)$, thereby considering the transition layer to be of negligible thickness (see Kaviany [47], and references therein). The above observation clearly indicates that the consideration of a transition layer is vital for a holistic description of the fluid-porous configuration. In addition, from a mathematical perspective, an important utility of the transition layer is that it serves as a regularization in between the Navier-Stokes and the Darcy equations, which do not have identical orders. Thus, it is evident that for modeling a dense or moderately porous medium (which constitutes the bulk proportion of different porous media encountered in various applications; highly porous media are few in proportion), neither Darcy nor Brinkman equation alone is sufficient for a proper representation of the porous layer. In spite of this, it is surprising that only a few studies have explored the role of this transition Brinkman porous layer in influencing the stability characteristics [48,49]. Hill *et al.* [48] carried out the analysis for a three-layer system (fluid layer, Brinkman transition layer, and Darcy layer), with homogeneous properties within each layer. On the other hand, Hill [49] considered a fluid layer, a heterogeneous Brinkman transition layer (with variable porosity and permeability), and a homogeneous Darcy layer (with constant porosity and permeability). These studies revealed that the depth of the transition layer is indeed an important parameter in affecting the stability characteristics of the flow system.

Apart from the analysis of transition to turbulence, the investigation of turbulent flow in porous media is also gaining the attention of the research community. Since this study is focused on the transition of flow to turbulence, a comprehensive review of the literature associated with the analysis of turbulent flow has not been undertaken. However, to illustrate an example, the readers are referred to the study conducted by Jimenez *et al.* [50]. They employed the eddy viscosity model in their direct numerical simulations for investigating the turbulent structures observed in a porous-walled channel characterized by an unstable mean velocity profile. It was revealed that coherent vortices originate at the interface of a porous layer owing to a Kelvin-Helmholtz (K-H) type shear instability.

A major limitation of all the aforementioned studies dealing with the transition layer is that they are confined to Newtonian fluids only, even though a majority of fluids encountered in real-life fluid-porous applications are non-Newtonian in nature. The appearance of the parameter characterizing the transition layer in the case of a non-Newtonian fluid is quite different from that of a Newtonian fluid (as would be later evident in the problem formulation part). Thus, it is essential to explore the

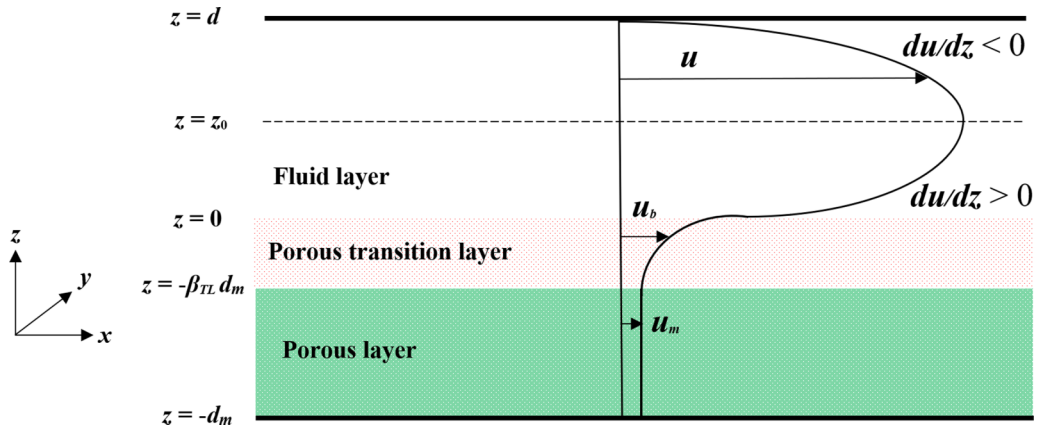

FIG. 1. Schematic for plane Poiseuille flow of a fluid overlying a porous layer: depiction of the three-layer flow configuration incorporating the porous transition layer (Brinkman layer) in between the unobstructed fluid layer and the porous layer (Darcy layer). u, u_b, u_m respectively refer to the velocities in the fluid layer, transition layer, and Darcy layer. Additionally, $z = z_0$ denotes the location where $\frac{du}{dz}$ changes its sign.

role of the transition porous layer in the case of non-Newtonian fluids. This is the major motivation behind the current study. Thus, in other words, it may be mentioned that most of the studies (dealing with fluid-porous combined flows) in the literature are limited to the selection of either the appropriate condition at the fluid-porous interface, or the appropriate governing equation for the porous layer. Furthermore, the studies concerned with the analysis of transition (hydrodynamic stability) for combined fluid-porous systems in channel flows are mostly limited to Newtonian fluids and the investigation of long-time (modal) flow transition characteristics. In this regard, the principal novelty of the present study lies in the fact that it attempts to capture the flow transition characteristics for a non-Newtonian fluid in the short-time (nonmodal) region, which is of great significance for bounded shear flows.

To begin with, the governing and the constitutive equations describing the flow are presented, and the basic velocity profiles are obtained in the three layers. Thereafter, modal analysis is carried out to assess the long-time behavior of the system. In addition to solving the non-Newtonian (power-law fluid) problem, the corresponding Newtonian problem for this flow configuration is also revisited. In doing so, a limitation of the earlier studies in assessing the true role of the transition layer on the flow transition characteristics is unveiled. In addition, nonmodal analysis is also attempted in order to estimate the short-time amplifications. An effort is made to identify the physical mechanism through which the criticality sets in.

II. PROBLEM FORMULATION

Figure 1 depicts a schematic of the flow configuration. A non-Newtonian fluid (modeled using power-law rheology) flows under an applied constant pressure gradient in a plane channel over a porous layer saturated with the same fluid. The porous layer consists of two zones: the layer at the bottom of the channel, and the transition layer existing in between the fluid layer and the bottom porous layer. The fluid layer is of thickness d (extending from $z = 0$ to $z = d$), whereas the porous layer (including the bottom layer and the transition layer) is of thickness d_m. The transition layer extends from $z = 0$ to $z = -\beta_{TL} d_m$, while the bottom layer extends from $z = -\beta_{TL} d_m$ to $z = -d_m$. Here, β_{TL} is a dimensionless parameter representing the depth of the transition layer. It is essentially the ratio of the transition layer depth to the total depth of the porous layer. It may be noted that $0 < \beta_{TL} < 1$, which takes care of all possible thicknesses of the transition layer relative to the porous layer beneath it. In fact, β_{TL} is typically in the range of 0.001–0.3 [48].

A. Governing equations

The governing Cauchy momentum equations in the fluid layer ($0 \leqslant z \leqslant d$) may be represented as

$$\nabla \cdot \boldsymbol{u} = 0, \tag{2.1a}$$

$$\rho \frac{D\boldsymbol{u}}{Dt} = -\nabla p + \nabla \cdot \boldsymbol{\tau}, \tag{2.1b}$$

where ρ is the density of the fluid, p is the pressure, and $\boldsymbol{u} \equiv (u, v, w)$ is the velocity vector. The deviatoric stress tensor $\boldsymbol{\tau}$ for a power-law fluid is given as

$$\boldsymbol{\tau} = \mu \dot{\boldsymbol{\gamma}} = \left(\mu^* \left| \sqrt{\frac{1}{2}(\dot{\boldsymbol{\gamma}} : \dot{\boldsymbol{\gamma}})} \right|^{n-1} \right) \dot{\boldsymbol{\gamma}}, \tag{2.2}$$

$\dot{\boldsymbol{\gamma}}$ being the rate of strain tensor, $\dot{\boldsymbol{\gamma}} = \nabla \boldsymbol{u} + (\nabla \boldsymbol{u})^T$, and μ is the power-law viscosity, $\mu = \mu^* |\sqrt{\frac{1}{2}(\dot{\boldsymbol{\gamma}} : \dot{\boldsymbol{\gamma}})}|^{n-1}$. μ^* and n are, respectively, the flow consistency and the flow behavior indices of the power-law fluid. Thus, by incorporating the rheology of the power-law fluid [from Eq. (2.2)], Eq. (2.1) may be expressed in scalar notation as

$$\frac{\partial u}{\partial x} + \frac{\partial v}{\partial y} + \frac{\partial w}{\partial z} = 0, \tag{2.3}$$

$$\rho\left(\frac{\partial u}{\partial t} + u\frac{\partial u}{\partial x} + v\frac{\partial u}{\partial y} + w\frac{\partial u}{\partial z}\right) = -\frac{\partial p}{\partial x} + \mu^*\left[\frac{\partial}{\partial x}\left\{M\left(2\frac{\partial u}{\partial x}\right)\right\} + \frac{\partial}{\partial y}\left\{M\left(\frac{\partial v}{\partial x} + \frac{\partial u}{\partial y}\right)\right\} + \frac{\partial}{\partial z}\left\{M\left(\frac{\partial u}{\partial z} + \frac{\partial w}{\partial x}\right)\right\}\right], \tag{2.4}$$

$$\rho\left(\frac{\partial v}{\partial t} + u\frac{\partial v}{\partial x} + v\frac{\partial v}{\partial y} + w\frac{\partial v}{\partial z}\right) = -\frac{\partial p}{\partial y} + \mu^*\left[\frac{\partial}{\partial x}\left\{M\left(\frac{\partial u}{\partial y} + \frac{\partial v}{\partial x}\right)\right\} + \frac{\partial}{\partial y}\left\{M\left(2\frac{\partial v}{\partial y}\right)\right\} + \frac{\partial}{\partial z}\left\{M\left(\frac{\partial v}{\partial z} + \frac{\partial w}{\partial y}\right)\right\}\right], \tag{2.5}$$

$$\rho\left(\frac{\partial w}{\partial t} + u\frac{\partial w}{\partial x} + v\frac{\partial w}{\partial y} + w\frac{\partial w}{\partial z}\right) = -\frac{\partial p}{\partial z} + \mu^*\left[\frac{\partial}{\partial x}\left\{M\left(\frac{\partial u}{\partial z} + \frac{\partial w}{\partial x}\right)\right\} + \frac{\partial}{\partial y}\left\{M\left(\frac{\partial v}{\partial z} + \frac{\partial w}{\partial y}\right)\right\} + \frac{\partial}{\partial z}\left\{M\left(2\frac{\partial w}{\partial z}\right)\right\}\right], \tag{2.6}$$

where $M = |2\{(\frac{\partial u}{\partial x})^2 + (\frac{\partial v}{\partial y})^2 + (\frac{\partial w}{\partial z})^2\} + \{(\frac{\partial u}{\partial y} + \frac{\partial v}{\partial x})^2 + (\frac{\partial u}{\partial z} + \frac{\partial w}{\partial x})^2 + (\frac{\partial v}{\partial z} + \frac{\partial w}{\partial y})^2\}|^{\frac{(n-1)}{2}}$.

In the above equations, $(u,\ v,\ w)$ denotes the velocity components in the fluid layer. It may be noted that although the above set of scalar equations, Eqs. (2.3)–(2.6), can be simplified while obtaining the base profile, it is necessary to consider the entire form in the derivation of the perturbation equations to be used in the stability analysis. Now, in the dense porous layer ($-d_m \leqslant z \leqslant -\beta_{TL} d_m$), the velocity is governed by the modified Darcy law for power-law fluids [51–53]:

$$\left.\begin{aligned} \nabla \cdot \boldsymbol{u}_m &= 0, \\ \left(\frac{\rho}{\varepsilon}\right)\frac{\partial \boldsymbol{u}_m}{\partial t} &= -\nabla p_m - \left(\frac{\mu^* |\boldsymbol{u}_m|^{n-1}}{K^*}\right)\boldsymbol{u}_m \end{aligned}\right\}, \tag{2.7}$$

where $\boldsymbol{u}_m$ is the seepage velocity vector. In scalar representation, the corresponding equations are

$$\frac{\partial u_m}{\partial x} + \frac{\partial v_m}{\partial y} + \frac{\partial w_m}{\partial z} = 0, \tag{2.8}$$

$$\left(\frac{\rho}{\varepsilon}\right)\frac{\partial u_m}{\partial t} = -\frac{\partial p_m}{\partial x} - \left[\frac{\mu^*\left(u_m^2 + v_m^2 + w_m^2\right)^{\frac{n-1}{2}}}{K^*}\right]u_m, \tag{2.9}$$

$$\left(\frac{\rho}{\varepsilon}\right)\frac{\partial v_m}{\partial t} = -\frac{\partial p_m}{\partial y} - \left[\frac{\mu^*\left(u_m^2 + v_m^2 + w_m^2\right)^{\frac{n-1}{2}}}{K^*}\right]v_m, \tag{2.10}$$

$$\left(\frac{\rho}{\varepsilon}\right)\frac{\partial w_m}{\partial t} = -\frac{\partial p_m}{\partial z} - \left[\frac{\mu^*\left(u_m^2 + v_m^2 + w_m^2\right)^{\frac{n-1}{2}}}{K^*}\right]w_m. \tag{2.11}$$

In Eqs. (2.9)–(2.11), ε denotes the porosity in the porous layer. p_m and $(u_m,\ v_m,\ w_m)$ respectively denote the pressure and velocity components in the Darcy layer, and K^* is the modified permeability, defined as

$$K^* = \frac{1}{2C_t}\left(\frac{n\varepsilon}{3n+1}\right)^n\left(\frac{50K}{3\varepsilon}\right)^{\frac{n+1}{2}}. \tag{2.12a}$$

The above equation may be expressed as

$$K^* = P_n K^{\frac{n+1}{2}}, \tag{2.12b}$$

where

$$P_n = \frac{1}{2C_t}\left(\frac{n\varepsilon}{3n+1}\right)^n\left(\frac{50}{3\varepsilon}\right)^{\frac{n+1}{2}}. \tag{2.12c}$$

In Eq. (2.12a), K is the intrinsic permeability of the porous media and is independent of the fluid rheology. In addition, C_t is the tortuosity factor, defined as [53]

$$C_t = \frac{2}{3}\left(\frac{8n}{9n+3}\right)^n\left(\frac{10n-3}{6n+1}\right)\left(\frac{75}{16}\right)^{\frac{3(10n-3)}{(10n+11)}}. \tag{2.12d}$$

The Brinkman model (also known as the Darcy-Brinkman model) is employed to model the flow in the porous transition layer ($-\beta_{TL}d_m \leqslant z \leqslant 0$). The modified form of the Brinkman model for power-law fluids may be given as [17]

$$\begin{gathered}\boldsymbol{\nabla}\cdot\boldsymbol{u}_b = 0,\\ \left(\frac{\rho}{\varepsilon}\right)\frac{\partial \boldsymbol{u}_b}{\partial t} = -\boldsymbol{\nabla}p_b - \left(\frac{\mu^*|\boldsymbol{u}_b|^{n-1}}{K^*}\right)\boldsymbol{u}_b + \frac{\mu^*}{\varepsilon^n}\boldsymbol{\nabla}\left\{\left|\sqrt{\frac{1}{2}(\boldsymbol{\Delta}:\boldsymbol{\Delta})}\right|^{n-1}\boldsymbol{\Delta}\right\}\end{gathered}\Bigg\}, \tag{2.13}$$

where $\boldsymbol{\Delta}$ is the rate of deformation tensor, defined as $\boldsymbol{\Delta} = \frac{1}{2}[(\boldsymbol{\nabla}\boldsymbol{u}_b) + (\boldsymbol{\nabla}\boldsymbol{u}_b)^T]$. In scalar notation, the corresponding equations are

$$\frac{\partial u_b}{\partial x} + \frac{\partial v_b}{\partial y} + \frac{\partial w_b}{\partial z} = 0, \tag{2.14}$$

$$\begin{aligned}\left(\frac{\rho}{\varepsilon}\right)\frac{\partial u_b}{\partial t} = &-\frac{\partial p_b}{\partial x} - \left[\frac{\mu^*\left(u_b^2 + v_b^2 + w_b^2\right)^{\frac{n-1}{2}}}{K^*}\right]u_b\\ &+ \frac{\mu^*}{\varepsilon^n}\left[\frac{\partial}{\partial x}\left\{M_b\left(2\frac{\partial u_b}{\partial x}\right)\right\} + \frac{\partial}{\partial y}\left\{M_b\left(\frac{\partial v_b}{\partial x} + \frac{\partial u_b}{\partial y}\right)\right\} + \frac{\partial}{\partial z}\left\{M_b\left(\frac{\partial u_b}{\partial z} + \frac{\partial w_b}{\partial x}\right)\right\}\right],\end{aligned} \tag{2.15}$$

$$\left(\frac{\rho}{\varepsilon}\right)\frac{\partial v_b}{\partial t} = -\frac{\partial p_b}{\partial y} - \left[\frac{\mu^*(u_b^2+v_b^2+w_b^2)^{\frac{n-1}{2}}}{K^*}\right]v_b + \frac{\mu^*}{\varepsilon^n}\left[\frac{\partial}{\partial x}\left\{M_b\left(\frac{\partial u_b}{\partial y}+\frac{\partial v_b}{\partial x}\right)\right\} + \frac{\partial}{\partial y}\left\{M_b\left(2\frac{\partial v_b}{\partial y}\right)\right\} + \frac{\partial}{\partial z}\left\{M_b\left(\frac{\partial v_b}{\partial z}+\frac{\partial w_b}{\partial y}\right)\right\}\right], \tag{2.16}$$

$$\left(\frac{\rho}{\varepsilon}\right)\frac{\partial w_b}{\partial t} = -\frac{\partial p_b}{\partial z} - \left[\frac{\mu^*(u_b^2+v_b^2+w_b^2)^{\frac{n-1}{2}}}{K^*}\right]w_b + \frac{\mu^*}{\varepsilon^n}\left[\frac{\partial}{\partial x}\left\{M_b\left(\frac{\partial u_b}{\partial z}+\frac{\partial w_b}{\partial x}\right)\right\} + \frac{\partial}{\partial y}\left\{M_b\left(\frac{\partial v_b}{\partial z}+\frac{\partial w_b}{\partial y}\right)\right\} + \frac{\partial}{\partial z}\left\{M_b\left(2\frac{\partial w_b}{\partial z}\right)\right\}\right], \tag{2.17}$$

where

$$M_b = \left|2\left\{\left(\frac{\partial u_b}{\partial x}\right)^2+\left(\frac{\partial v_b}{\partial y}\right)^2+\left(\frac{\partial w_b}{\partial z}\right)^2\right\} + \left\{\left(\frac{\partial u_b}{\partial y}+\frac{\partial v_b}{\partial x}\right)^2+\left(\frac{\partial u_b}{\partial z}+\frac{\partial w_b}{\partial x}\right)^2 + \left(\frac{\partial v_b}{\partial z}+\frac{\partial w_b}{\partial y}\right)^2\right\}\right|^{\frac{(n-1)}{2}}. \tag{2.18}$$

In addition, p_b and $(u_b,\ v_b,\ w_b)$ denote the pressure and the velocity components in the Brinkman transition layer.

B. Boundary conditions

Upon observing Eq. (2.4), it is easy to understand that the final form of the momentum equation will depend on the sign of $\frac{\partial u}{\partial z}$. This is where the behavior of a power-law fluid is fundamentally different from that of a Newtonian fluid. $z = z_0$ is the location where $\frac{\partial u}{\partial z}$ undergoes a change in sign. Now, the various applicable boundary conditions are to be listed. To begin with, the continuity of normal stresses is assumed at the two interfaces (at $z = 0$ and $z = -\beta_{TL}d_m$), leading to the following conditions at the interfaces:

$$\text{at } z = 0, \quad -p + 2\mu^* M\left(\frac{\partial w}{\partial z}\right) = -p_b + 2\left(\frac{\mu^*}{\varepsilon^n}\right)M_b\left(\frac{\partial w_b}{\partial z}\right), \tag{2.19a}$$

$$\text{at } z = -\beta_{TL}d_m, \quad -p_m = -p_b + 2\left(\frac{\mu^*}{\varepsilon^n}\right)M_b\left(\frac{\partial w_b}{\partial z}\right). \tag{2.19b}$$

It is worthwhile to mention that Eqs. (2.19a) and (2.19b) do not imply that there is a discontinuity of pressure at the two interfaces. Essentially, the pressure is interpreted as a pore-averaged pressure in the porous medium. Hence, Eqs. (2.19a) and (2.19b) are consistent with the notion of continuity of pressure at the microscopic level. A similar approach has also been followed by Hill and Straughan [48]. To formulate the other boundary conditions, the upper wall of the channel is considered. Assuming no-slip at the upper wall,

$$\text{at } z = d, \quad u = 0, \quad v = 0, \quad w = 0. \tag{2.20}$$

Next, the boundary conditions valid at the fluid layer–transition layer interface need to be listed. The continuity of velocities is applicable at the interface between the fluid layer and the transition layer, i.e.,

$$\text{at } z = 0, \quad u = u_b, \quad v = v_b, \quad w = w_b. \tag{2.21}$$

In addition to the continuity of velocities, the continuity of tangential stresses is maintained at the interface between the fluid layer and the transition Brinkman layer. In mathematical terms,

$$\text{at } z=0, \quad \begin{cases} \mu^*\left[M\left(\frac{\partial u}{\partial z}+\frac{\partial w}{\partial x}\right)\right]=\left(\frac{\mu^*}{\varepsilon^n}\right)\left[M_b\left(\frac{\partial u_b}{\partial z}+\frac{\partial w_b}{\partial x}\right)\right], \\ \mu^*\left[M\left(\frac{\partial v}{\partial z}+\frac{\partial w}{\partial y}\right)\right]=\left(\frac{\mu^*}{\varepsilon^n}\right)\left[M_b\left(\frac{\partial v_b}{\partial z}+\frac{\partial w_b}{\partial y}\right)\right], \\ \mu^*\left[M\left(\frac{\partial u}{\partial y}+\frac{\partial v}{\partial x}\right)\right]=\left(\frac{\mu^*}{\varepsilon^n}\right)\left[M_b\left(\frac{\partial u_b}{\partial y}+\frac{\partial v_b}{\partial x}\right)\right]. \end{cases} \tag{2.22}$$

The Beavers-Joseph condition prevails at the interface between the transition Brinkman layer and the Darcy layer for the streamwise and the spanwise velocities [48,54]. For a power-law fluid, it assumes the form [55,56]

$$\text{at } z=-\beta_{TL}d_m, \quad \begin{cases} \left(\frac{\partial u_b}{\partial z}\right)=\frac{\alpha_{BJ}(u_b-u_m)}{K^{*\frac{1}{n+1}}}, \\ \left(\frac{\partial v_b}{\partial z}\right)=\frac{\alpha_{BJ}(v_b-v_m)}{K^{*\frac{1}{n+1}}}, \end{cases}$$

where α_{BJ} is the Beavers-Joseph constant. Physically, α_{BJ} signifies the slip coefficient at the interface. Upon substituting the expression of K^* [using Eq. (2.12b)],

$$\text{at } z=-\beta_{TL}d_m, \quad \begin{cases} \left(\frac{\partial u_b}{\partial z}\right)=\frac{\alpha_{BJ}(u_b-u_m)}{P_n^{\frac{1}{n+1}}\sqrt{K}}, \\ \left(\frac{\partial v_b}{\partial z}\right)=\frac{\alpha_{BJ}(v_b-v_m)}{P_n^{\frac{1}{n+1}}\sqrt{K}}. \end{cases} \tag{2.23a}$$

As far as the normal velocity is concerned, continuity is maintained. Mathematically, this translates to

$$\text{at } z=-\beta_{TL}d_m, \quad w_b=w_m. \tag{2.23b}$$

Finally, at the bottom wall (end of the porous layer), impermeability is assumed, i.e.,

$$\text{at } z=-d_m, \quad v_m=0, \quad w_m=0. \tag{2.24}$$

III. ANALYSIS OF THE BASE VELOCITY PROFILE

A. Base velocity profile

The base flow is assumed to be laminar, steady, fully developed, and unidirectional (it is a function of z only). The base velocities in the three layers are obtained by the solution of the governing equations subject to the above boundary conditions. The following length scales are used for nondimensionalization: d in the fluid layer and d_m in the porous layer, i.e., $\bar{z}=z/d$ for $0\leqslant z\leqslant d$, and $\bar{z}_m=z/d_m$ for $-d_m\leqslant z\leqslant 0$. In addition, the velocity scale used for nondimensionalization is the maximum velocity in the fluid layer, $u_{\max}$. Therefore, in the fluid layer ($0\leqslant\bar{z}\leqslant 1$), the nondimensional velocity profiles may be expressed as

$$\begin{aligned} &\bar{u}=1-\left(\frac{|\bar{z}_0-\bar{z}|}{1-\bar{z}_0}\right)^{\frac{n+1}{n}}, \quad \text{for } 0\leqslant\bar{z}\leqslant 1; \\ &\bar{v}=0, \quad \bar{w}=0, \quad \text{for } 0\leqslant\bar{z}\leqslant 1. \end{aligned} \tag{3.1}$$

In the Brinkman transition layer ($-\beta_{TL}\leqslant\bar{z}_m\leqslant 0$), the corresponding expressions are

$$\begin{aligned} &\frac{d^2\bar{u}_b}{d\bar{z}_m^2}-A\left(\frac{d\bar{u}_b}{d\bar{z}_m}\right)^{1-n}\bar{u}_b^n+B\left(\frac{d\bar{u}_b}{d\bar{z}_m}\right)^{1-n}=0, \quad \text{for } -\beta_{TL}\leqslant\bar{z}_m\leqslant 0; \\ &\bar{v}_b=0, \quad \bar{w}_b=0, \quad \text{for } -\beta_{TL}\leqslant\bar{z}_m\leqslant 0, \end{aligned} \tag{3.2}$$

where

$$A=\left(\frac{\varepsilon^n}{n}\right)\left[\frac{1}{P_n\,\delta^{n+1}}\right], \quad B=\left(\frac{n+1}{n}\right)^n\left(\frac{\varepsilon^n}{n}\right)\left(\frac{1}{\hat{d}^{n+1}}\right)\left[\frac{1}{(1-\bar{z}_0)^{n+1}}\right]. \tag{3.3}$$

It may be noted that it is not possible to obtain an explicit algebraic expression for $\bar{u}_b$, unlike the case of the fluid layer velocity $\bar{u}$. Finally, in the porous Darcy layer situated at the bottom of the channel ($-1 \leqslant \bar{z}_m \leqslant -\beta_{TL}$), the velocity profiles may be expressed as

$$\bar{u}_m = \left[\left(\frac{\delta}{\hat{d}}\right)^{n+1}\left(\frac{n+1}{n}\right)^{n}\left(\frac{1}{(1-\bar{z}_0)^{n+1}}\right)P_n\right]^{\frac{1}{n}}, \quad \text{for } -1 \leqslant \bar{z}_m \leqslant -\beta_{TL};$$
$$\bar{v}_m = 0, \ \bar{w}_m = 0, \quad \text{for } -1 \leqslant \bar{z}_m \leqslant -\beta_{TL}. \tag{3.4}$$

In the above nondimensional forms, several important nondimensional parameters emerge. One of such important parameters is the depth ratio $\hat{d} = (d/d_m)$, signifying the relative thicknesses of the fluid and the porous layers. Also, $\delta = \sqrt{K}/d_m$ is the Darcy number, being a nondimensional measure of permeability of the porous layer. It is evident that an exact analytical solution of the velocity profile is not possible in the present problem, unlike that for a Newtonian fluid. Thus, numerical methods are employed for the purpose. The numerical scheme used for obtaining the velocity profiles is outlined in Appendix A.

B. Results and discussion

1. Newtonian rheology ($n = 1$)

Throughout the current study, the following values are assumed for describing the porous media (unless otherwise explicitly stated): $\alpha_{BJ} = 0.1$, $\varepsilon = 0.3$, $\hat{d} = 0.1$, $\delta = 10^{-5}$. These values are well within the range prescribed in earlier studies [25,29,48]. Initially, the flow configuration studied by Hill and Straughan [48] involving a Newtonian fluid is revisited. In the beginning, the base velocity profiles are analyzed. Figure 2 depicts the impact of the depth of the transition layer (quantified by β_{TL}) on the base velocity profile. Three representative values of β_{TL} have been considered. Out of these, the case corresponding to $\beta_{TL} = 0.1$ has been explicitly considered by Hill and Straughan [48]. The same has been shown in Fig. 2(a) (rectangular data points refer to the results by Hill and Straughan [48]), and it matches with our computation, thereby serving as a validation of the present approach as well. Hill and Straughan [48] and Hill [49] opined that one of the major reasons for considering a three-layer configuration (involving a transition layer) instead of the traditional two-layer approach (adopted by Chang, Chen, and Straughan [25], and many others thereafter) is to eradicate the discontinuity of velocity at the interface. It is indeed observable from their plot (refer to Fig. 2 of Hill and Straughan [48]) that there is no significant velocity discontinuity at the interface of the Brinkman transition layer and the Darcy layer. However, the velocity profile was plotted by them [48] only for $\beta_{TL} = 0.1$ (despite the fact that the neutral stability curves were plotted for a wide spectrum of β_{TL} values ranging from 0.001 to 0.3). For a better understanding of the impact of β_{TL}, two more values of β_{TL} (0.001 and 0.05) have been considered in the present work. It is interesting to notice from Fig. 2(c) that for $\beta_{TL} = 0.001$, there is a significant velocity discontinuity at the interface of the Darcy layer and the Brinkman layer [i.e., at $\bar{z}_m = -\beta_{TL} = -0.001$; this is clearly depicted in the inset in Fig. 2(c)]. Thus, the continuity of velocities is valid only when the depth of the transition layer is comparatively larger. Therefore, the simplistic assumption made by them [48] that the velocity discontinuity can be removed effectively by considering a transition layer is not entirely correct. Here, it may be worthwhile to clarify that no velocity discontinuity is obtained at $z = 0$ for any value of β_{TL}, in coherence with Eq. (2.21).

Moreover, it may be noticed that there is no decay of velocity within the bottom porous layer, which is contradictory to the results of Bruneau and Mortazavi [13,14]. The reason for the same is attributed to the difference in the model equations used to describe the porous layer. Since the entire porous layer is modeled using the Brinkman equation (which has a viscous diffusion term in the formulation) in their studies [13,14], there is a decay between the channel wall (at $\bar{z}_m = -1$) and the Brinkman-Darcy interface (at $\bar{z}_m = -\beta_{TL}$). On the other hand, only the transition layer is modeled by the Brinkman equation in the present analysis. The rest of the porous layer is modeled by the Darcy equation, where the aforementioned decay cannot be present owing to the constant

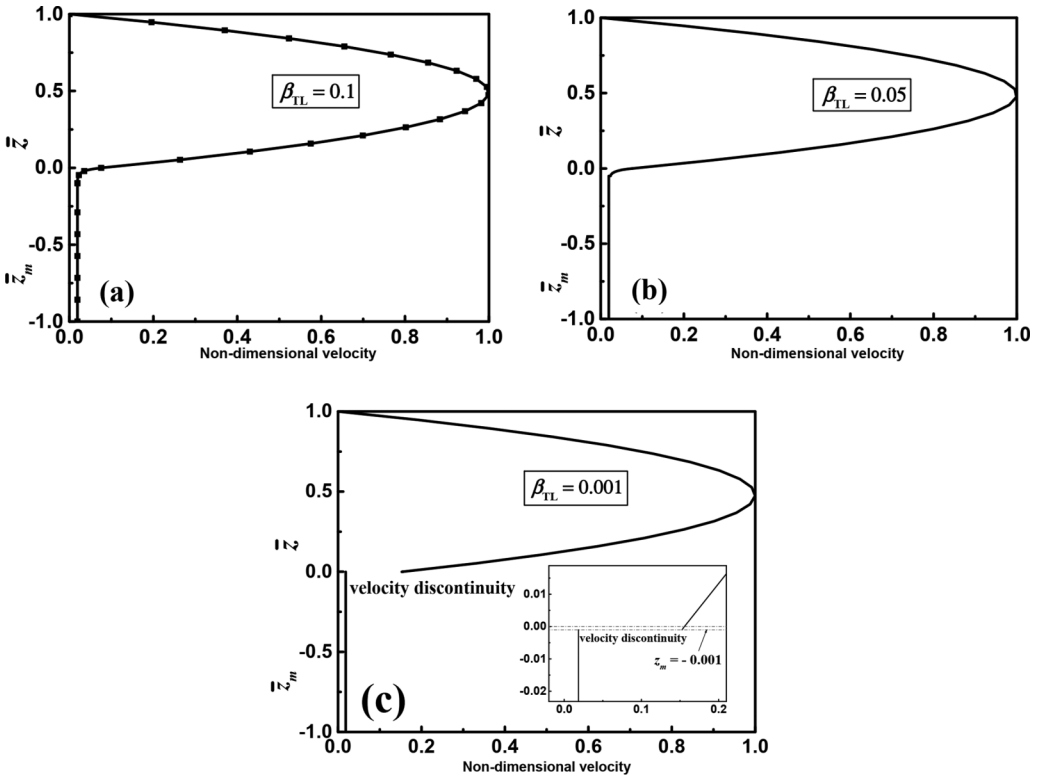

FIG. 2. Nondimensional velocity profiles in the three layers as a function of the depth of the transition layer β_{TL} for the flow of a Newtonian fluid ($n = 1$). (a), (b), and (c) are plotted for $\beta_{TL} = 0.1$, 0.05, and 0.001, respectively. In (a), a comparison is also made with the velocity profile obtained by Hill and Straughan [48], depicted by rectangular symbols. A significant velocity discontinuity is visible at the Darcy-Brinkman interface for (c). The inset in (c) depicts the point of discontinuity. Other parameters are $\hat{d} = 0.1$, $\varepsilon = 0.3$, $\delta = 2.5 \times 10^{-5}$, $\alpha_{BJ} = 0.1$.

velocity in the porous layer. The Brinkman equation could not be employed throughout the porous matrix, as a porous layer of low porosity (<0.4) has been assumed, while the Brinkman equation is applicable only when the porosity is close to unity (as considered by [13,14] in their investigations). Other researchers whose approach is analogous to the present study also did not observe any such decay [48].

2. Power-law rheology ($n \neq 1$)

Now, the velocity profiles for the power-law rheology are demonstrated in Fig. 3. Figure 3(a) depicts the effect of β_{TL} for a shear-thinning fluid ($n = 0.3$), while Fig. 3(b) does the same for a shear-thickening fluid ($n = 1.5$). It may be observed that akin to Newtonian fluids, there is a gradual reduction in the velocity discontinuity with β_{TL}, for both shear-thinning and shear-thickening fluids. In other words, as the depth of the transition layer increases, the effect of the velocity discontinuity is gradually diminished. The reason behind the same has already been elucidated while discussing the case of Newtonian fluids. One interesting observation is that for a shear-thinning fluid, the effect of β_{TL} on the porous layer velocity is more prominent in comparison to that of a shear-thickening fluid. At the chosen scale of the plots, it is even difficult to distinguish between different porous layer velocities in Fig. 3(b). Therefore, it may be said that the shear-thinning rheology better amplifies the effect of the transition layer on the flow behavior in the porous layer. This interplay between

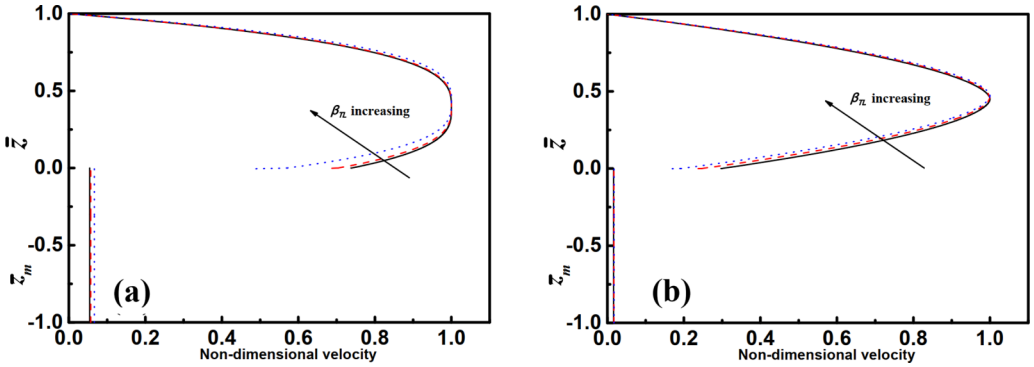

FIG. 3. Nondimensional velocity profiles in the three layers to illustrate the effect of the depth of the transition layer β_{TL} for a (a) shear-thinning fluid ($n = 0.3$), (b) shear-thickening fluid ($n = 1.5$). The following values of β_{TL} are considered in each case: $\beta_{TL} = 0.001, 0.01, 0.05$.

the shear-thinning rheology and the transition layer depth will be explored in more detail in the succeeding sections while analyzing the flow stability.

IV. STABILITY ANALYSIS

A. Theoretical framework

After analyzing the base profiles, an analysis of hydrodynamic stability is undertaken as it is the principal motive of the present study. It is known that an equivalent of Squire's theorem does not exist for a fluid with nonlinear viscosity (as is the case for power-law and other similar classes of non-Newtonian fluids) [57]. Therefore, there is a need to undertake a rigorous three-dimensional stability analysis. In the beginning, an infinitesimal disturbance $(\boldsymbol{u}', \boldsymbol{u_b}', \boldsymbol{u_m}', p')$ is imparted to the base flow $(\bar{\boldsymbol{u}}, \bar{\boldsymbol{u}}_b, \bar{\boldsymbol{u}}_m, \bar{p})$, where $\boldsymbol{u}' = (u', v', w')$, $\boldsymbol{u_b}' = (u_b', v_b', w_b')$, $\boldsymbol{u_m}' = (u_m', v_m', w_m')$, etc. Thereafter, the governing equations for the base state are subtracted from those for the perturbed state, and the perturbation equations are made nondimensional. The approach followed for nondimensionalization is analogous to the one adopted by Hill and Straughan [48]. As a result, the following initial value problem is obtained for the fluid layer:

$$i(\alpha\hat{u} + \beta\hat{v}) + D\hat{w} = 0, \tag{4.1a}$$

$$\frac{\partial\hat{u}}{\partial t} = -i\alpha\bar{u}\hat{u} - \hat{w}D\bar{u} - i\alpha\hat{p} + \frac{1}{\mathrm{Re}}[\bar{\mu}(D^2 - \alpha^2 - \beta^2)\hat{u} + D\mu_t(D\hat{u} + i\alpha\hat{w}) + (\mu_t - \bar{\mu})(D^2\hat{u} + i\alpha D\hat{w})], \tag{4.1b}$$

$$\frac{\partial\hat{v}}{\partial t} = -i\alpha\bar{u}\hat{v} - i\beta\hat{p} + \frac{1}{\mathrm{Re}}[\bar{\mu}(D^2 - \alpha^2 - \beta^2)\hat{v} + D\bar{\mu}(D\hat{v} + i\beta\hat{w})], \tag{4.1c}$$

$$\frac{\partial\hat{w}}{\partial t} = -i\alpha\bar{u}\hat{w} - D\hat{p} + \frac{1}{\mathrm{Re}}[\bar{\mu}(D^2 - \alpha^2 - \beta^2)\hat{w} + 2D\bar{\mu}D\hat{w} + (\mu_t - \bar{\mu})i\alpha(D\hat{u} + i\alpha\hat{w})], \tag{4.1d}$$

where, $D = d/dz$, and the Reynolds number Re is expressed as $\mathrm{Re} = \frac{\rho u_{\max}^{2-n} d^n}{\mu^*}$. α and β denote the streamwise and the spanwise wave numbers of the perturbation waves. In the above equations, the tangent viscosity μ_t is defined as [58]

$$\mu_t = \bar{\mu} + \left.\frac{d\mu}{d\dot{\gamma}_{zx}}\right|_{u=\bar{u}} \bar{\dot{\gamma}}_{zx}. \tag{4.2}$$

Essentially, the departure of the viscosity of a non-Newtonian fluid from the Newtonian counterpart is quantified by $(\mu_t - \bar{\mu})$. For a power-law fluid,

$$\mu_t - \bar{\mu} = (n-1)\bar{\dot{\gamma}}^{n-1}. \tag{4.3}$$

Proceeding in a similar fashion, the initial value problem for the Brinkman porous layer is obtained as

$$i(\alpha_b \hat{u}_b + \beta_b \hat{v}_b) + D_b \hat{w}_b = 0, \tag{4.4a}$$

$$\frac{\partial \hat{u}_b}{\partial t_b} = -\left(\frac{\varepsilon}{\mathrm{Re}_b}\right)\Bigg[i\alpha_b \hat{p}_b + \frac{n}{P_n}\cdot\frac{\bar{u}_b^{n-1}}{\delta^{n+1}}\cdot\hat{u}_b - \frac{1}{\varepsilon^n}\{\Omega\,\hat{u}_b + D_b\mu_{tb}(D_b\hat{u}_b + i\alpha_b\hat{w}_b) + D_b\,\Gamma_b\}\Bigg], \tag{4.4b}$$

$$\frac{\partial \hat{v}_b}{\partial t_b} = -\left(\frac{\varepsilon}{\mathrm{Re}_b}\right)\Bigg[i\beta_b \hat{p}_b + \frac{1}{P_n}\cdot\frac{\bar{u}_b^{n-1}}{\delta^{n+1}}\cdot\hat{v}_b - \frac{1}{\varepsilon^n}\{\Omega\hat{v}_b + D_b\bar{\mu}_b(D_b\hat{v}_b + i\beta_b\hat{w}_b)\}\Bigg], \tag{4.4c}$$

$$\frac{\partial \hat{w}_b}{\partial t_b} = -\left(\frac{\varepsilon}{\mathrm{Re}_b}\right)\Bigg[D_b\hat{p}_b + \frac{1}{P_n}\cdot\frac{\bar{u}_b^{n-1}}{\delta^{n+1}}\cdot\hat{w}_b - \frac{1}{\varepsilon^n}\{\Omega\hat{w}_b + 2D_b\bar{\mu}_b D_b\hat{w}_b + i\alpha_b\Gamma_b\}\Bigg], \tag{4.4d}$$

where $\Omega_b = \bar{\mu}_b({D_b}^2 - {\alpha_b}^2 - {\beta_b}^2)$, $\Gamma_b = (\mu_{tb} - \bar{\mu}_b)(D_b\hat{u}_b + i\alpha_b\hat{w}_b)$. Lastly, the initial value problem for the Darcy layer is presented as

$$i(\alpha_m \hat{u}_m + \beta_m \hat{v}_m) + D_m \hat{w}_m = 0, \tag{4.5a}$$

$$\frac{\partial \hat{u}_m}{\partial t_m} = -\left(\frac{\varepsilon}{\mathrm{Re}_m}\right)\left(i\alpha_m \hat{p}_m + \frac{n}{P_n}\cdot\frac{\bar{u}_m^{n-1}}{\delta^{n+1}}\cdot\hat{u}_m\right), \tag{4.5b}$$

$$\frac{\partial \hat{v}_m}{\partial t_m} = -\left(\frac{\varepsilon}{\mathrm{Re}_m}\right)\left(i\beta_m \hat{p}_m + \frac{1}{P_n}\cdot\frac{\bar{u}_m^{n-1}}{\delta^{n+1}}\cdot\hat{v}_m\right), \tag{4.5c}$$

$$\frac{\partial \hat{w}_m}{\partial t_m} = -\left(\frac{\varepsilon}{\mathrm{Re}_m}\right)\left(D_m\hat{p}_m + \frac{1}{P_n}\cdot\frac{\bar{u}_m^{n-1}}{\delta^{n+1}}\cdot\hat{w}_m\right), \tag{4.5d}$$

where the Reynolds number in the Darcy layer Re_m is defined as $\mathrm{Re}_m = \frac{\rho u_m^{2-n} d_m^n}{\mu^*}$.

B. Numerical methodology

The disturbance equations and the boundary conditions corresponding to the modal analysis have been provided in Appendix B. In order to undertake modal analysis, the resultant eigenvalue problem $\boldsymbol{AX} = c\boldsymbol{BX}$ is solved in MATLAB via the Chebyshev spectral collocation method. Here, $\boldsymbol{X} = (u, v, w, p)$, and $\boldsymbol{A}$, $\boldsymbol{B}$ are the matrices involving the Chebyshev derivative terms. The associated detailed numerical methodology regarding the same may be found in Schmid and Henningson [59]. The results obtained for this work have been computed with $N = 160$, where N is the number of Chebyshev polynomials. With this value of N, the eigenvalues could be obtained with an accuracy of five digits.

Now, the methodology for carrying out nonmodal analysis is outlined. Nonmodal analysis is an indispensable tool to obtain insights into the transient amplifications of a flow configuration that is not unveiled by modal analysis, which aims at capturing only the long-time characteristics. This is especially important in the context of viscous channel flows, for which the results obtained from modal analysis often fail to predict experimental findings owing to the non-normal characteristic of the corresponding Orr-Sommerfeld operator [60]. For undertaking nonmodal analysis, a solution to

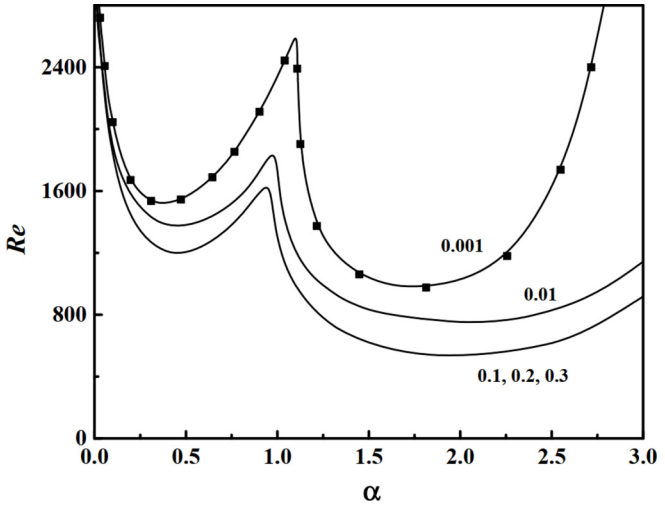

FIG. 4. Neutral stability curves for a streamwise perturbation ($\beta = 0$) in the case of a Newtonian fluid ($n = 1$) for different values of the transition layer depth β_{TL}. The values of β_{TL} are shown against the respective curves in each case. A comparison with the existing literature is carried out for $\beta_{TL} = 0.001$, where the solid circles refer to the data points obtained from Hill and Straughan [48].

the following linear initial value problem is sought:

$$\frac{\partial}{\partial t}\boldsymbol{q} = -i\boldsymbol{L}\boldsymbol{q}. \tag{4.6}$$

In the above problem, $\boldsymbol{q} = (\hat{u},\ \hat{v},\ \hat{w},\ \hat{p})^T$, $\boldsymbol{L} = -i\boldsymbol{B}^{-1}\boldsymbol{A}$. Thus, the solution may be expressed as $\boldsymbol{q}(t) = \exp(-i\boldsymbol{L}t)\,\boldsymbol{q}(0)$, where $\boldsymbol{q}(0)$ refers to the initial value of the perturbation variables. With regard to Eq. (4.6), growth function $G(t)$ quantifies the maximum possible amplification of $q(0)$, i.e., the initial condition. Mathematically, it may be expressed as

$$G(t) = \max_{q(0)\neq 0} \frac{\|\boldsymbol{q}(t)\|^2}{\|\boldsymbol{q}(0)\|^2} = \|e^{-i\boldsymbol{L}t}\|^2, \tag{4.7}$$

where $\|\cdot\|$ is the norm [60]. In this regard, the maximum growth $G_{\max}$ is basically the growth function maximized over time, and the corresponding time at which $G_{\max}$ is attained is referred to as $t_{\max}$. Therefore, in mathematical terms,

$$G_{\max} = G(t_{\max}) = \max G(t), \quad t \geqslant 0. \tag{4.8}$$

C. Results and discussion

1. Newtonian rheology

As a follow-up to the analysis of base velocity profiles (carried out in Sec. III), the impact of β_{TL} on the flow stability is analyzed now. The neutral stability curves are constructed for the purpose, where the critical Reynolds number is plotted against the wave number of a streamwise perturbation (i.e., the spanwise wave number $\beta = 0$) (refer to Fig. 4). It is found that β_{TL} has a significant effect on the criticality only when it is small ($\beta_{TL} < 0.01$). A comparison of our results with the literature [48] corresponding to $\beta_{TL} = 0.001$ is also carried out, so as to validate our methodology and computation. A satisfactory match between the two is observed. For $\beta_{TL} = 0.1$ and beyond (at which the velocity discontinuity is effectively removed, as observed in Fig. 2), there is no significant impact of β_{TL} on the flow criticality. Although this effect was visible in one of the plots in Hill and Straughan [48], no concrete discussion or insight on the same was available. However, this

is important in order to understand the role played by the transition layer. Thus, in the case of a Newtonian fluid, the argument that the transition layer is able to eradicate the velocity discontinuity and influence the flow stability simultaneously is not justified. When the transition layer is able to influence flow stability, a discontinuity prevails in the velocity profile. On the other hand, when the discontinuity is curbed, there is no significant influence of the transition layer on the flow transition behavior. This is probably due to the fact that in a fluid-porous system, the flow stability is influenced significantly by the porous modes at the interface [25]. A suppression of the velocity discontinuity (via a choice of high β_{TL}) reduces the influence of the porous modes to a large extent, thereby imparting a negligible effect on the neutral stability curve. Thus, while dealing with a practical configuration involving a Newtonian fluid-porous system, it is vital to realize that the transition layer will influence flow stability only when its thickness is small. If the thickness of the transition layer increases beyond 10% of the total thickness of the porous layer, any further variation in its thickness would not dictate the flow transition. The actual depth of the transition layer for a flow system depends on the fluid and the porous medium. It is a complex function of several hydrodynamic parameters, and no exact quantification of the same exists in the literature to date. However, once the depth of the transition layer is measured (as is normally done through experiments), it would be possible to comment whether flow stability is affected by that depending on its magnitude relative to the total depth of the porous layer.

2. Power-law rheology: Long-time characteristics

Having realized the role of the transition layer in the case of a Newtonian fluid, the attention is now shifted to power-law rheology. At first, neutral stability curves are constructed to depict the mutual interaction between the transition layer and the power-law rheology in dictating the long-time linear stability characteristics. Figures 5(a)–5(d) depict the role played by the depth of the transition layer β_{TL} on the critical Reynolds number for a streamwise perturbation (i.e., for which the spanwise wave number $\beta = 0$), while Figs. 6(a)–6(d) demonstrate the same for a spanwise perturbation (i.e., for which the streamwise wave number $\alpha = 0$). In Fig. 5(a), it is found that with an increase in the flow behavior index n from 0.3 to 1.5 (i.e., as the fluid turns from shear-thinning to shear-thickening), there is a monotonic increase in the magnitude of critical Re. This indicates that the flow turns stable as we proceed from shear-thinning to shear-thickening characteristics. The same behavior is observed even for higher values of β_{TL} up to 0.08 [in Figs. 5(a)–5(d)]. It has been found that as β_{TL} is increased beyond 0.08, there is no appreciable change in either the magnitude or the nature of the plots (not depicted here). The multimodal nature of the neutral curves is attributed to the interplay of the fluid and the porous modes. An interesting observation is that although there is a monotonic lowering of both the short-wave (high wave number) fluid modes and the long-wave (small wave number) porous modes with increasing shear-thinning behavior in Fig. 5(a), the same trend is not replicated in the rest of the cases [Figs. 5(b)–5(d)]. In other words, as the depth of the transition layer increases, there is a complex interplay between the power-law rheology (characterized by n) and the transition layer, owing to which the porous mode does not follow a monotonic pattern of criticality. The same, however, is not reflected in the fluid mode, which shows a monotonic lowering with decreasing n irrespective of the magnitude of depth of the transition layer. This occurs because the critical disturbance waves originating in the fluid layer do not become dominated by the transition layer. However, the shearing (quantified by the rheology, and consequently, by the flow behavior index n) action is the influencing factor.

An analogous trend is demonstrated even in the case of spanwise perturbations [in Figs. 6(a)–6(d)], although a lower critical Re is observed for the corresponding values of n and β_{TL} in each case. This shows that a spanwise perturbation triggers criticality faster than a streamwise perturbation.

Figure 7 depicts the values of critical Reynolds number $\mathrm{Re}_{\mathrm{cr}}$ [in Fig. 7(a)] and critical spanwise wave number β_{cr} [in Fig. 7(b)] versus n in each case over a range of permeability values. Darcy number δ, which is a nondimensional measure of permeability, varies from 5×10^{-5} to 5×10^{-4} (for more details on the typical range of δ, one may refer to Hill and Straughan [48]). It is observed

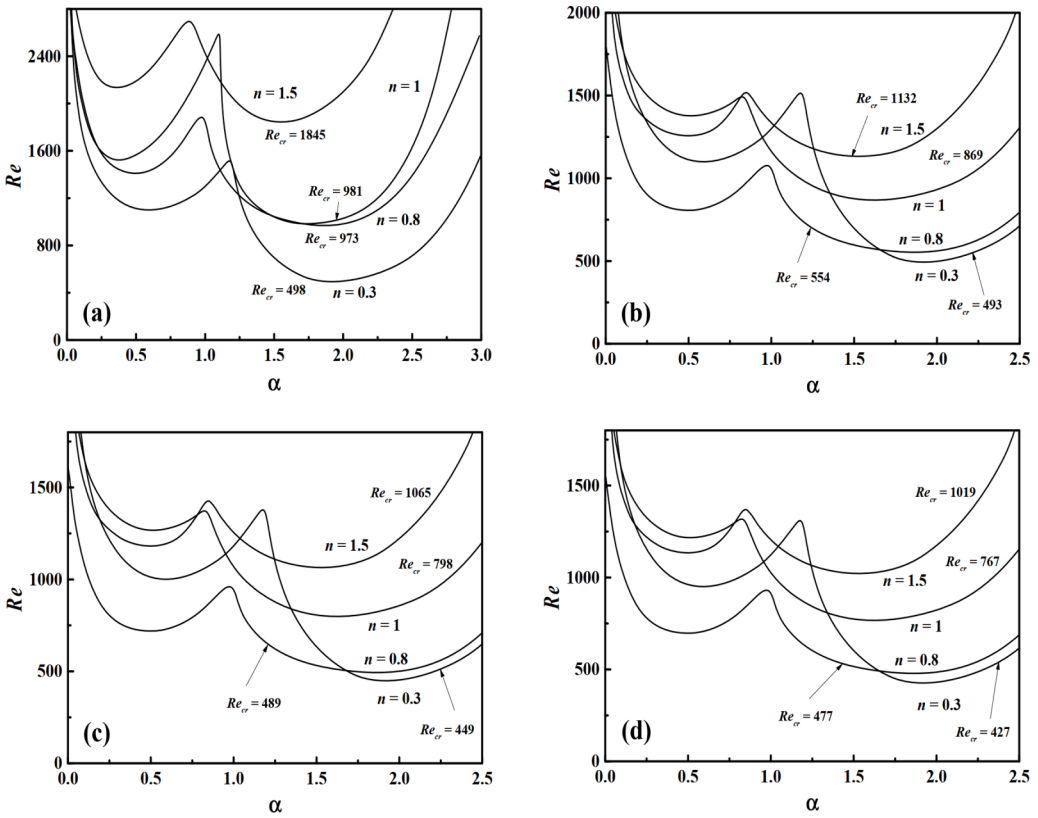

FIG. 5. Neutral stability curves for a streamwise perturbation ($\beta = 0$) depicting the effect of the flow behavior index n on the critical Reynolds number for different values of the transition layer depth β_{TL}. (a) $\beta_{TL} = 0.001$, (b) $\beta_{TL} = 0.01$, (c) $\beta_{TL} = 0.05$, (d) $\beta_{TL} = 0.08$. The value of the critical Reynolds number $\mathrm{Re_{cr}}$ corresponding to the dominant mode of instability is also mentioned against the curves in each case.

that $\mathrm{Re_{cr}}$ decreases monotonically with δ, signifying the destabilizing role of the permeability. This is possibly because of the fact that an increased permeability enhances the fluid movement in the porous layer, thereby triggering the porous modes to initiate flow transition [25]. On the other hand, the critical wave number β_{cr} is found to increase with δ (for a fixed n), thereby indicating the dominance of short waves in dictating the flow transition. The effect of n on $\mathrm{Re_{cr}}$ is reverse to that exhibited by δ, thereby signifying that as we proceed from shear-thinning to shear-thickening behavior, the flow is gradually stabilized. These conflicting trends exhibited by the Darcy number and the flow behavior index are indeed interesting, as this feature can be suitably exploited to either trigger or delay flow transition in the designing of a fluid-porous system. A judicious selection of appropriate values of δ and n can either trigger the onset of flow transition (large δ, small n), or delay the transition (small δ, large n). In fact, it is possible to tune the system by deciding upon the Re (based on what one desires to achieve), and then appropriately select δ and n based on whether it is required to maintain laminar flow or not. For example, if mixing is desirable in an industrial application, one would like to trigger the flow transition to enhance the convective heat and mass transport. A large value of δ and small n are selected in such a scenario.

It may be noted that Fig. 7 shows only the critical values of Re and wave number. It does not exhibit the interaction of fluid and porous modes by depicting the multimodal neutral curves, unlike Figs. 5 and 6. This is because in the current study, our focus has been to develop a fundamental understanding of the role played by the transition layer in altering the flow transition characteristics.

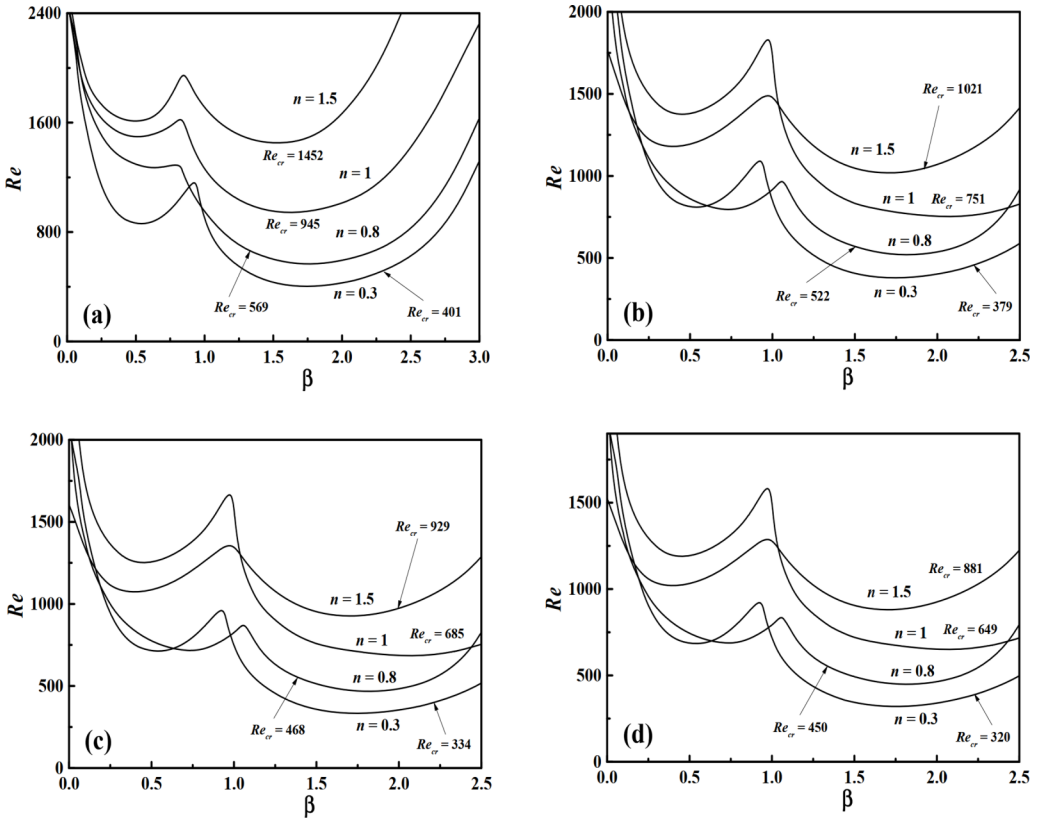

FIG. 6. Neutral stability curves for a spanwise perturbation ($\alpha = 0$) depicting the effect of the flow behavior index n on the critical Reynolds number for different values of the transition layer depth β_{TL}. (a) $\beta_{TL} = 0.001$, (b) $\beta_{TL} = 0.01$, (c) $\beta_{TL} = 0.05$, (d) $\beta_{TL} = 0.08$. The value of the critical Reynolds number $\mathrm{Re_{cr}}$ corresponding to the dominant mode of instability is also mentioned against the curves in each case.

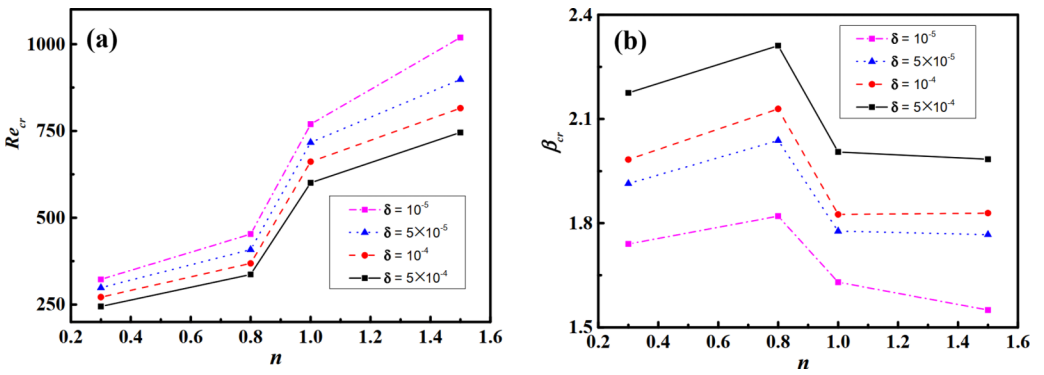

FIG. 7. Effect of the flow behavior index n on the modal stability for different values of Darcy number δ. A spanwise perturbation ($\alpha = 0$) has been considered for the purpose. (a) Plot of critical Reynolds number $\mathrm{Re_{cr}}$ versus n. (b) Plot of critical spanwise wave number β_{cr} versus n. The values of δ are specified against the respective plots in each case. $\beta_{TL} = 0.08$ is taken for all the plots.

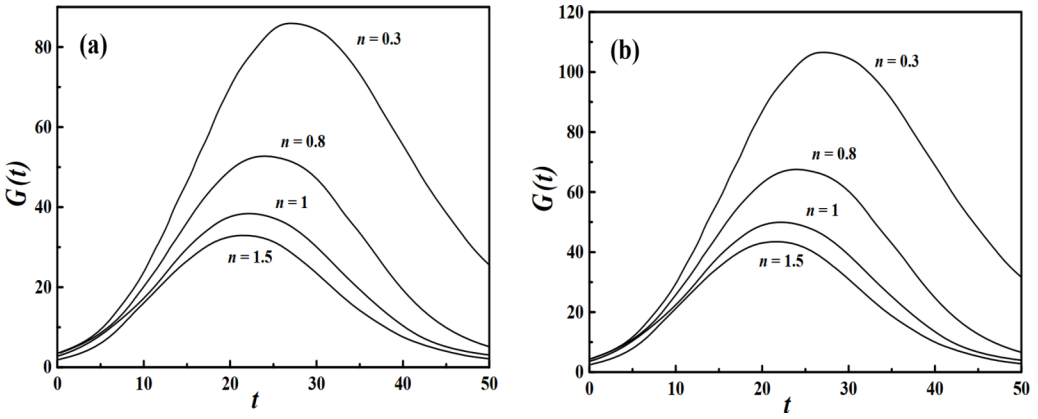

FIG. 8. Growth rate curves for a streamwise perturbation with $\alpha = 1$, Re $= 200$ depicting the effect of the flow behavior index n for different values of the transition layer depth β_{TL}. (a) $\beta_{TL} = 0.001$, (b) $\beta_{TL} = 0.08$.

We aim to do so by thoroughly analyzing the effect of the transition layer on various aspects of modal and nonmodal growth. Owing to this, showing the effects of other important parameters of the porous layer like porosity, permeability, depth ratio, etc., is not the motive in this work. Nevertheless, a small study is incorporated (as illustrated in Fig. 7) regarding the interplay between the Darcy number δ (which is a nondimensional measure of permeability) and the power-law rheology (through n), to demonstrate the benefits that may be derived out of a fluid-porous system by the pertinent tuning of relevant parameters. However, a detailed analysis involving all the aforementioned porous layer parameters would be accommodated in a future study.

3. Power-law rheology: Short -time characteristics

Now, it would be interesting to observe the nonmodal transient growth behavior and the impacts of the transition layer and the fluid rheology on the same. Figure 8 depicts the growth rate curves for a streamwise perturbation. From Fig. 8(a), for $\beta_{TL} = 0.001$, it is found that the initial growth rate (i.e., $\frac{dG}{dt}|_{t=0}$) does not depend significantly on the magnitude of n. However, the growth is amplified as the fluid becomes strongly shear-thinning and in fact, this trend is monotonic. In addition, the time at which the maximum growth is realized increases with decrease in n (i.e., as the fluid becomes more shear-thinning). In other words, a shear-thinning fluid has to be weakly shear-thinning if the transient amplifications arising from streamwise disturbances need to be reduced. As β_{TL} is increased to 0.08 in Fig. 8(b), the streamwise disturbances cause greater amplifications, leading to an augmentation in $G(t)$. The monotonic behavior with n is restored here as well.

Figure 9 depicts the transient growth characteristics for a spanwise perturbation. Greater amplifications are observed here compared to the case of streamwise perturbations, hinting at the dominant role played by the spanwise perturbations in transient growth. Physically, it indicates that a spanwise perturbation wave would cause greater energy amplifications at finite time, triggering chances of secondary instability in viscous boundary layer flows, causing augmented turbulence and hence mixing [61]. In addition, a significant deviation from Fig. 8 is revealed here. It is observed that the effect of flow behavior index on the transient growth is not always monotonic as the fluid turns strongly shear-thinning. While the variation with n is strictly monotonic for low depth of the transition layer [$\beta_{TL} = 0.001$ in Fig. 9(a)], the scenario is reversed as the depth increases [$\beta_{TL} = 0.08$ in Fig. 9(b)] for the cases $n = 0.3$ and $n = 0.8$. This hints at a competitive interplay between the transition layer and the fluid rheology in deciding the fate of the spanwise amplifications.

In order to obtain a holistic understanding of the features of transient growth and to have a possible explanation of the nonmonotonic behavior observed in the case of shear-thinning fluids at

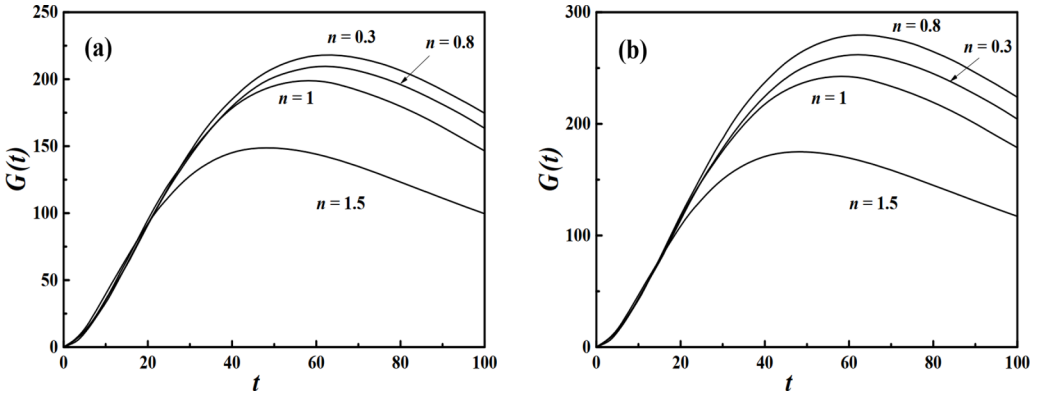

FIG. 9. Growth rate curves for a spanwise perturbation with $\beta = 2$, Re $= 200$ depicting the effect of the flow behavior index n for different values of the transition layer depth β_{TL}. (a) $\beta_{TL} = 0.001$, (b) $\beta_{TL} = 0.08$.

high β_{TL}, the contours of maximum growth $G_{\max}$ are depicted in Figs. 10 (corresponding to the case of $n = 0.3$) and 11 (corresponding to $n = 0.8$) for a vast range of wave numbers on the (α, β) plane. In this regard, the optimal energy growth is defined as

$$G_{\text{opt}} = \max_{\alpha,\,\beta} G_{\max}(\alpha, \beta), \quad \text{at } t = t_{\text{opt}}. \tag{4.9}$$

The corresponding perturbation (quantified by the values of α and β) achieving G_{opt} is known as the optimal perturbation. Figure 10(a) depicts that for $n = 0.3$, the optimal perturbation corresponds to a spanwise disturbance when the transition layer is thin, while it becomes oblique (albeit with a low α) at a large β_{TL} in Fig. 10(b). As the degree of shear-thinning decreases (n increases) in Fig. 11, the optimal perturbations are found to be spanwise for both low and high β_{TL}. In other words, when the transition layer is of small depth, the nature of optimal perturbations is similar (spanwise) across different degrees of shear-thinning. However, as the transition layer thickness grows to a higher magnitude, the optimal perturbation turns from oblique to spanwise with n. As spanwise perturbations are known to cause greater amplifications, a purely spanwise optimal perturbation [in Fig. 11(b)] exceeds an oblique perturbation [in Fig. 10(b)] in dominating the transient amplifications. The same gets manifested in the form of a higher magnitude of nonmodal growth for the former. From the perspective of flow physics, this increases chances of subcritical

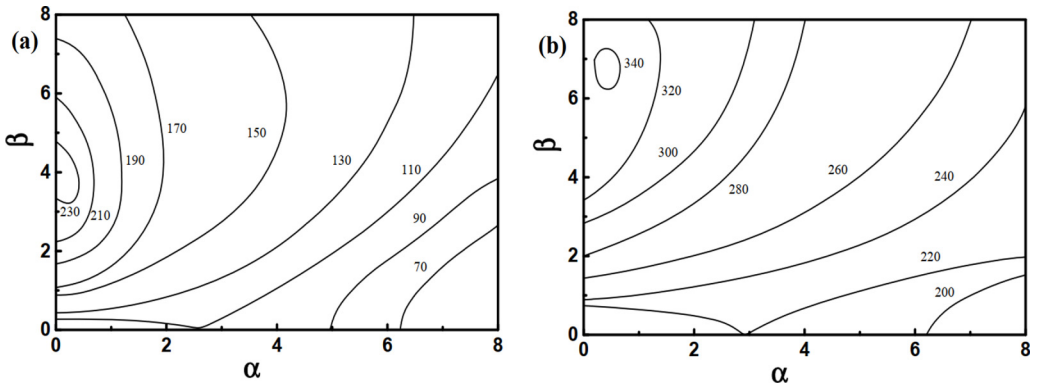

FIG. 10. Contours of maximum growth $G_{\max}$ on the (α, β) plane for $n = 0.3$ for (a) $\beta_{TL} = 0.001$, (b) $\beta_{TL} = 0.08$. Re $= 200$ in both cases.

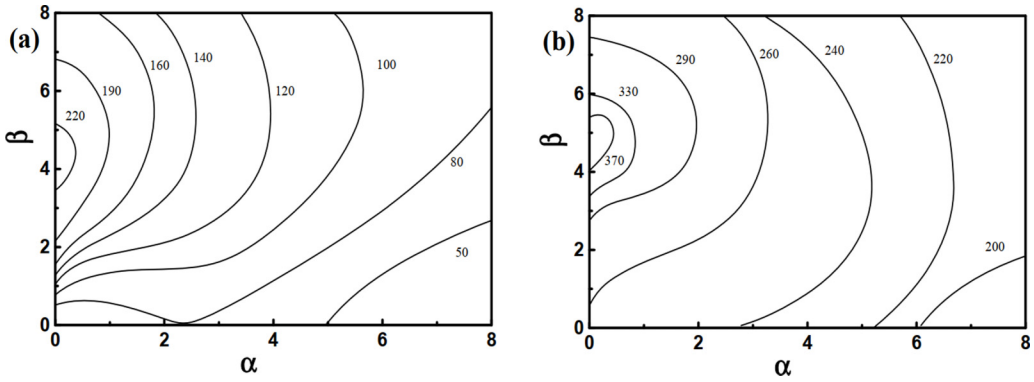

FIG. 11. Contours of maximum growth $G_{\max}$ on the (α, β) plane for $n = 0.8$ for (a) $\beta_{TL} = 0.001$, (b) $\beta_{TL} = 0.08$. Re $= 200$ in both cases.

transition in bounded shear flows even though long-time modal instability may be absent [60]. This differential response to a variation in β_{TL} depending on the intensity of shear-thinning indicates the need for determination of the order of magnitude of transition layer thickness. It is possible to obtain drastically different flow transition behavior for the same shear-thinning fluid in a fluid-porous system, depending on the depth of the transition layer. Thus, in a suitable industrial application where there may be avenues to engineer the porous media to obtain the desired flow transition behavior (either advance or delay flow transition), one of the important parameters while selecting the porous medium should be the thickness of the transition layer that is formed when the process fluid comes in contact with the medium. The above consideration would aid strategic designing of flow parameters in a fluid-porous industrial system based on the requirement of either triggering or delaying flow transition.

When the fluid is shear-thickening, as considered in Fig. 12 for $n = 1.5$, the optimal perturbation remains spanwise irrespective of whether the transition layer depth β_{TL} is small [as in Fig. 12(a)] or large [Fig. 12(b)]. Thus, there is no qualitative impact on the nature of optimal perturbation waves, even though the magnitude of nonmodal growth varies, as is expected. Computations with even higher values of n (up to $n = 1.8$; plots are not supplied here to avoid repetition) have been carried out, but the same trend has been observed throughout. Thus, for shear-thickening fluids, the nonmodal response (quantified as energy growth) to change in transition layer depth is always

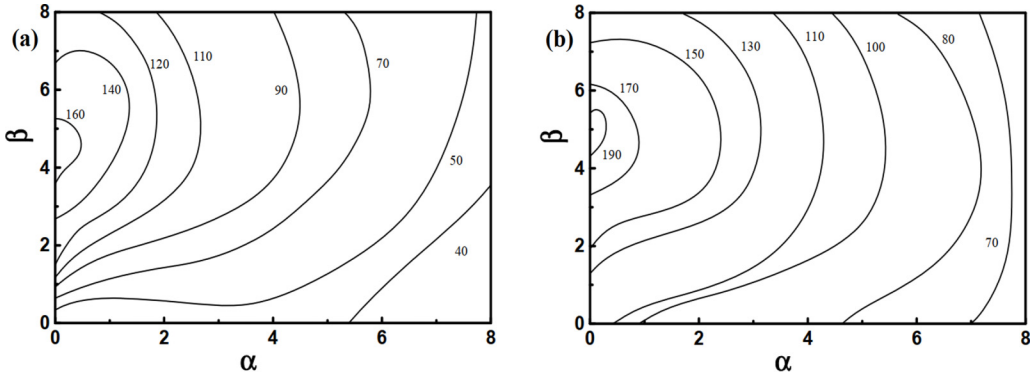

FIG. 12. Contours of maximum growth $G_{\max}$ on the (α, β) plane for $n = 1.5$ for (a) $\beta_{TL} = 0.001$, (b) $\beta_{TL} = 0.08$. Re $= 200$ in both cases.

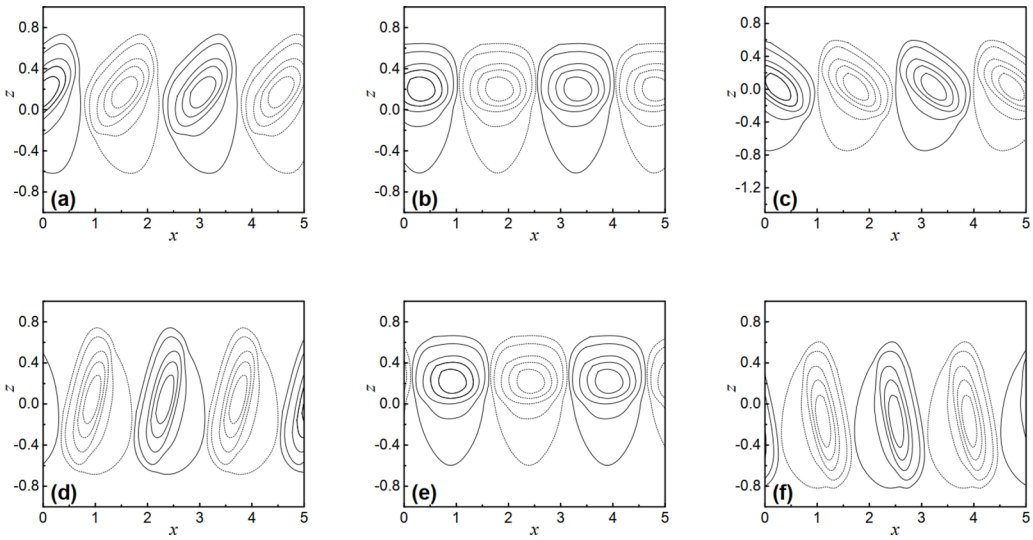

FIG. 13. Flow patterns for the optimal perturbation in the case of a shear-thinning fluid ($n = 0.5$). (a), (b), (c) correspond to $\beta_{TL} = 0.001$, while (d), (e), (f) correspond to $\beta_{TL} = 0.08$. (a), (d) represent the flow field at initial time ($t = 0$); (b), (e) represent the flow field at optimal time ($t = t_{\text{opt}}$); (c), (f) represent the flow field at $t = 1.3t_{\text{opt}}$. The contour levels from outer to inner represent the values of u in the following order: 0.1, 0.3, 0.5, 0.7, 0.9. Re $= 200$ throughout.

monotonic, unlike its shear-thinning counterpart. From a design perspective, this revelation has significant implications in deciding the flow transition characteristics of a fluid-porous configuration. Therefore, if the fluid under consideration is shear thickening in nature, one can conveniently anticipate that the flow would be monotonically destabilizing with transition layer depth, irrespective of the intensity of shear thickening. On the contrary, when the fluid is shear-thinning, the flow transition behavior is not monotonic with transition layer depth, owing to the complex interplay between the shear-thinning characteristics and the transition layer. Thus, in such a scenario, the degree of shear-thinning has a prominent effect on the resultant flow transition characteristics.

4. Physical mechanism dictating flow transition

In order to comprehend the fundamental physical mechanism governing the nonmodal growth behavior, the temporal evolution of the perturbation flow field is explored in Figs. 13 (shear-thinning) and 14 (shear-thickening). Figures 13(a)–13(c) depict the case when $\beta_{TL} = 0.001$, while Figs. 13(d)–13(f) represent the case when $\beta_{TL} = 0.08$. The flow patterns exhibit a streaklike shape. It is observed from Fig. 13(a) that at initial time, the flow field is tilted in a direction opposite to that of the mean shear flow. This can be explained by the Reynolds stress mechanism. The opposite orientation (tilting) is because the disturbance wave extracts energy from the mean shear flow. Physically, this energy extraction leads to a rise in the magnitude of nonmodal growth, as already demonstrated in Figs. 8 and 9. At optimal time [Figs. 13(b)], there is an upright orientation owing to no further extraction of energy from the mean shear flow. As the thickness of the transition layer is increased in Fig. 13(d), there is a visibly greater degree of tilting of the perturbation flow field compared to that in Fig. 13(a). This behavior is probably because an increase in the transition layer thickness makes the fluid-fluid viscous interaction more significant, thereby augmenting the available energy pool in the mean shear flow for the disturbance to extract from. If we observe the behavior of the disturbance fields after the optimal time [in Figs. 13(c) and 13(f)], they are found to tilt toward the streamwise direction. This contrasting orientation (as compared to the behavior at $t = 0$) signifies the release of energy to the mean shear flow.

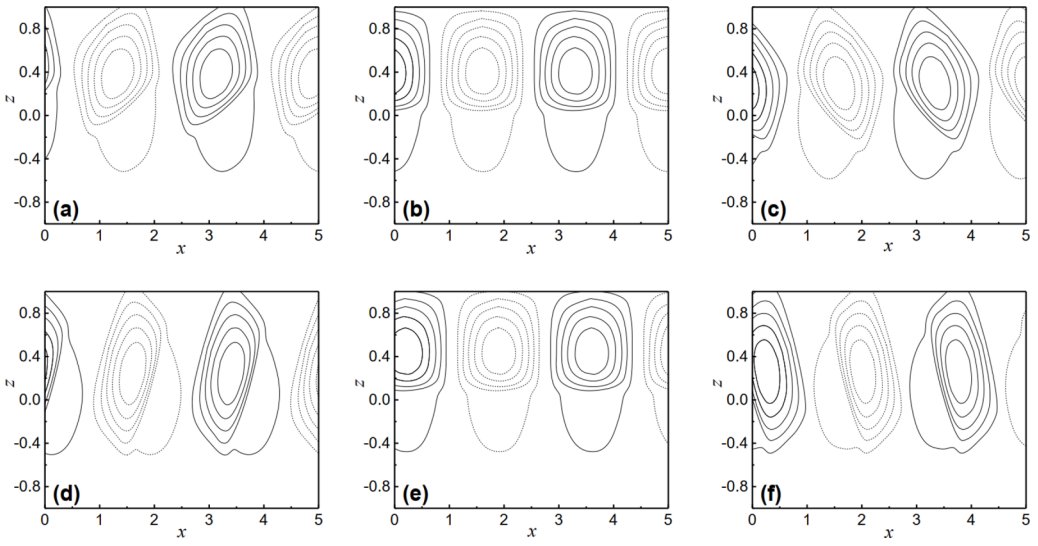

FIG. 14. Flow patterns for the optimal perturbation in the case of a shear-thickening fluid ($n = 1.3$). (a), (b), (c) correspond to $\beta_{TL} = 0.001$, while (d), (e), (f) correspond to $\beta_{TL} = 0.08$. (a), (d) represent the flow field at initial time ($t = 0$); (b), (e) represent the flow field at optimal time ($t = t_{\text{opt}}$); (c), (f) represent the flow field at $t = 1.3t_{\text{opt}}$. The contour levels from outer to inner represent the values of u in the following order: 0.1, 0.3, 0.5, 0.7, 0.9. Re $= 200$ throughout.

Although the flow patterns for the temporal evolution of the disturbance field in the case of a shear-thickening fluid (in Fig. 14) are found to exhibit qualitative similarities (for example, tilting opposite to the mean shear flow at $t = 0$) to that of a shear-thinning fluid, there are two notable differences. The first one is that there is less protrusion of the disturbance into the porous layer. A reduced protrusion hints at a drop in the fluid-fluid viscous interactions within the transition layer, consequently explaining the reduction in transient growth as compared to the shear-thinning case (as was observed in Figs. 8 and 9). The second contrast is that there is a significant increase in the spacing between the streaks, compared to the shear-thinning case. The enhancement in streak spacing may be attributed to coalescence between neighboring streaks, leading to a reduction in transient energy [62]. Thus, the synergistic effects of these two contrasting factors explain the significant variations between the transient growths of shear-thickening and shear-thinning fluids in the context of a fluid-porous channel flow configuration. Consequently, shear-thickening fluids exhibit a lower magnitude of transient energy growth compared to the shear-thinning one.

V. CRITICAL ASSESSMENT BASED ON EXISTING LITERATURE, AND FUTURE PROSPECTS

The authors would like to state that while both the current work as well as the ones by Hill and Straughan [48] and Hill [49] deal with a transition layer in a fluid-porous configuration, there are significant differences among these. The principal difference between the present study and the earlier studies [48,49] is that the present study deals with nonmodal analysis in addition to the traditional eigenvalue analysis (modal analysis), while the earlier ones [48,49] were limited to classical modal analysis. Nonmodal analysis is extremely crucial for investigating the short-time amplifications (that might lead to subcritical transition) in shear flows, as the associated operator is non-normal in nature [59,60]. Modal analysis fails to anticipate such possibilities of subcritical transition in shear flows; hence nonmodal analysis is known to predict experimental observations of flow transition better under such circumstances [59].

Therefore, the novelty in the current study (as compared to the earlier ones [48,49]) is not limited to the consideration of a power-law fluid. In fact, the major highlight of the current work is that it attempts to capture the role of the transition layer toward dictating the nonmodal flow transition characteristics, which is important in shear flow configurations (like the one considered in the present study), and this issue was not addressed by earlier studies [48,49]. A power-law fluid is considered for a more accurate simulation of real-life non-Newtonian flow rheology frequently observed in natural and industrial applications. To the best of our knowledge, no study has been reported in the literature (either for a Newtonian or a non-Newtonian fluid) that investigates the effect of the transition layer toward influencing the nonmodal flow stability characteristics.

While a porous layer involves several important parameters such as porosity, permeability (Darcy number), relative thickness (depth ratio), etc., the objective of the current study has been to understand the interplay between the fluid rheology (quantified by n) and the relative thickness of the transition layer (quantified by β_{TL}). Therefore, with the help of modal and nonmodal analyses, an attempt is made to unveil the intricate interplay between n and β_{TL}.

However, the authors still felt that it may be worthwhile to throw some light on the influence of at least another porous layer parameter in the context of non-Newtonian rheology, in order to appreciate the significant influence of the porous layer on flow stability. Due to this, Fig. 7 has been incorporated to exhibit the interplay between permeability (Darcy number) and flow rheology (n) in the context of modal analysis only. We did not attempt nonmodal analysis for investigating the effect of permeability, so as to remain focused on the objective of this study, i.e., the effects of the transition layer on flow stability.

As far as the depth ratio is concerned, its effect has not been analyzed at all in this study, as depth ratio has been one of the most studied parameters in the literature in the context of hydrodynamic stability of Newtonian fluid-porous systems. However, it is acknowledged that the effects of the depth ratio and other parameters (like porosity and permeability) on the flow stability of a non-Newtonian fluid is largely unexplored, particularly in the context of nonmodal analysis. We plan to incorporate these in a future study.

It has already been highlighted that a crucial aspect regarding the modeling of fluid-porous flow is the appropriate selection of the governing equations corresponding to each of fluid and porous domains, and the choice of a suitable interface condition for connecting the two domains. In this regard, Ochoa-Tapia and Whitaker [63] proposed an interfacial jump condition (also known as the OTW condition) based on the nonlocal form of the volume-averaged Stokes equation. An adjustable parameter is present in their model that requires experimental determination. The OTW condition deviates from the Beavers-Joseph condition (that has been considered in the present study), as it assumes stress jump and velocity continuity, while the latter assumes a velocity jump and a stress continuity. The major advantage of the approach suggested by [63] is that it allows us to use the classical partial differential equations for both the fluid (Cauchy momentum equation) and the porous (Brinkman equation) domains. However, the Brinkman equation is typically suited for porous media with a very high porosity (close to unity) [20]. Since the present study is concerned with porous media of low to moderate density (less than 0.4), a combination of the Darcy layer (for the bottom porous layer) and the Beavers-Joseph condition (for describing the interface of the transition layer and the bottom porous layer) has been adopted. A future study involving a highly porous media can possibly consider the Brinkman equation throughout the entire porous layer along with the OTW condition at the fluid-porous interface.

On another front, it may be noted that the base velocity fields have been analyzed in detail toward the beginning of this article. As far as the base pressure fields are concerned, it is worthwhile to highlight that we have considered a constant applied pressure gradient in the current study. Owing to this, the base pressure profile would be linear. As a result, the base pressure profile is not expected to have a significant influence on the hydrodynamic stability of Poiseuille flows, and thus has not been explored frequently in such scenarios [25,27,29,48,59,64,65]. Hence, the plots of pressure fields have not been included in the present study. However, the authors acknowledge that this assumption is simplistic, as a linear pressure profile cannot be maintained in several applications of

practical interest involving fluid-porous systems. Taking this into consideration, we aim to pursue an analysis in future where the pressure profile varies nonlinearly along the channel length. The plots of pressure fields would possibly provide better understanding of the flow transition behavior in such a scenario.

VI. CONCLUSION

The present work entailed two important objectives. The first objective is related to the revisit of the Newtonian problem in the chosen flow configuration. Although Hill and Straughan [48] and Hill [49] claimed in their studies that the nondimensional Brinkman layer depth parameter β_{TL} has a significant effect on the instability of the flow configuration, the statement is perhaps not entirely correct in absolute terms. A small value of β_{TL} leads to velocity discontinuity at the Darcy-Brinkman interface. Hill and Straughan [48] advocated a β_{TL} of 0.1 and above, as this forces the discontinuity of the velocity profile at the interface of the transition (Brinkman) layer and the porous (Darcy) layer to become numerically insignificant. However, even though Hill and Straughan [48] advocated a choice of $\beta_{TL} > 0.1$ for ensuring continuity of velocity at the interface of the transition layer and the Darcy layer, there is no significant effect on the neutral stability curves for $\beta_{TL} > 0.1$ for a Newtonian fluid. Since β_{TL} has a visible effect on the neutral stability curves only for small values (when it lies in the range [0.001, 0.05]), it is perhaps not correct to consider the transition layer as a parameter that simultaneously enforces continuity of velocity at the interface and controls the flow stability characteristics. Thus, one interesting revelation of the current work is that the effect of β_{TL} on the flow transition characteristics is not that significant when the discontinuity of the velocity profile disappears. In fact, the variation in transition layer depth is able to influence the criticality only when there is a numerical discontinuity in the velocity profile at the interface. This reinforces the statement that the onset of criticality is heavily dictated by the discontinuity at the fluid-porous interface, and it is difficult to avoid the same by consideration of a transition layer. Nevertheless, this may turn out to be a boon, and one can make suitable exploitation of this phenomenon to tune criticality based on the requirements (for example, enhanced mixing for facilitating convective transport in certain industrial applications).

The second objective is related to the consideration of a power-law rheology. A need was felt to explore the effect of the transition layer in the case of a non-Newtonian fluid, as a majority of the fluids that are encountered in fluid-porous systems in natural and industrial scenario exhibit non-Newtonian flow characteristics. The governing equations describing the flow in the transition porous layer are highly nonlinear for a power-law fluid, thereby yielding no possibility of an analytical solution. Thus, in the current study, a somewhat semianalytical approach had to be adopted to obtain the velocity profiles in the three layers (fluid layer, transition layer, and porous layer). The inherent nonlinear rheology of a power-law fluid leads to several complexities, which also affect the fluid-porous interface characteristics and, consequently, the flow physics of the system. Analogously to a Newtonian fluid, it is observed that there exists a threshold $\beta_{TL} = 0.08$, beyond which there is no appreciable change in flow transition characteristics. The shear-thinning behavior is always found to impart flow destabilization in the exponential (long-time) domain. In the short-time (zone of algebraic growth) domain, however, the situation is not monotonic. For a shear-thinning fluid, when the transition layer is thin (low β_{TL}), shear-thinning is monotonically destabilizing. However, when β_{TL} is large, it is not so. A possible explanation for the same is derived from the contours of $G_{\max}$, wherein the optimal perturbations are found to be streamwise-independent at low β_{TL}, while they turn oblique at high β_{TL}. The shear-thickening fluids, however, exhibit monotonic behavior with the flow behavior index n. The transient behavior is explained by tracking the temporal evolution of the disturbance flow fields and comprehending the underlying physical mechanism responsible for the same. All these insights are important from design considerations, as already discussed.

Thus, in a nutshell, the current study attempted to demonstrate the necessity to consider a transition layer while modeling the fluid-porous flow configuration (especially in the contexts of hydrodynamic stability and non-Newtonian rheology), by highlighting its dominant effect via the

development of a fundamental framework. The findings from the study will possibly encourage further investigations in this area.

APPENDIX A: NUMERICAL METHODOLOGY FOR THE CALCULATION OF THE VELOCITY PROFILES

It has already been stated in the main article that an exact analytical solution is not possible in the case of the present flow configuration. Although it may seem that exact analytical expressions are provided for fluid layer velocity $\bar{u}$ and Darcy velocity $\bar{u}_m$ [in Eqs. (3.1) and (3.4), respectively], it may be observed that both of these contain $\bar{z}_0$, which is an unknown parameter. Moreover, no such explicit expression exists for Brinkman velocity $\bar{u}_b$; it is represented via a differential equation [Eq. (3.2)].

In this context, it is important to highlight the nondimensional boundary conditions (BCs) used for obtaining the velocity profiles:

(i) $$\text{at } \bar{z} = 1, \quad \bar{u} = 0, \tag{A1}$$

(ii) $$\text{at } \bar{z} = \bar{z}_m = 0, \quad \bar{u} = \bar{u}_b, \tag{A2}$$

(iii) $$\text{at } \bar{z} = \bar{z}_m = 0, \quad \frac{d\bar{u}}{d\bar{z}} = \left(\frac{\hat{d}}{\varepsilon}\right)\left(\frac{d\bar{u}_b}{d\bar{z}_m}\right), \tag{A3}$$

(iv) $$\text{at } \bar{z}_m = -\beta_{TL}, \quad \frac{d\bar{u}_b}{d\bar{z}_m} = \frac{\alpha_{BJ}(\bar{u}_b - \bar{u}_m)}{P_n^{\frac{1}{n+1}}\,\delta}. \tag{A4}$$

It may be noted that the BC given by Eq. (A1) has already been used while evaluating the expression of the velocity profile in the fluid layer $\bar{u}$; therefore the same cannot be used any further. Thus, we focus our attention on the rest of the boundary conditions [Eqs. (A2)–(A4)]. From Eqs. (A2) and (A3), we obtain

$$\bar{u}_b|_{\bar{z}_m=0} = 1 - \left(\frac{\bar{z}_0}{1-\bar{z}_0}\right)^{\frac{n+1}{n}}, \tag{A5}$$

$$\left.\frac{d\bar{u}_b}{d\bar{z}_m}\right|_{\bar{z}_m=0} = \left(\frac{\varepsilon}{\hat{d}}\right)\left(\frac{n+1}{n}\right)\left(\frac{1}{1-\bar{z}_0}\right)\left(\frac{\bar{z}_0}{1-\bar{z}_0}\right)^{\frac{1}{n}}. \tag{A6}$$

Thus, the first line of Eq. (3.2), together with BCs given by Eqs. (A5) and (A6), constitute an initial value problem of an ordinary differential equation (ODE-IVP), that may be solved by numerical techniques (an implicit algorithm based on the Adams-Moulton method has been adopted for the purpose in this study). But, that too requires a knowledge of $\bar{z}_0$. Thus, the following scheme is outlined for the evaluation of the velocity profiles in the three layers:

(i) Assume a value of $\bar{z}_0$ ($0 < \bar{z}_0 < 1$).

(ii) Calculate $\bar{u}$ and $\bar{u}_m$ using the first lines of Eq. (3.1) and Eq. (3.4), respectively, and solve the initial value problem [first line of Eq. (3.2) together with Eqs. (A5) and (A6)] to obtain $\bar{u}_b$.

(iii) Check whether Eq. (A4) is satisfied (i.e., the left and the right hand sides of the equation match) within an acceptable accuracy limit (10^{-5}). If not, go to step (i) and re-choose a value of $\bar{z}_0$. Otherwise, stop and report the values of $\bar{u}$, $\bar{u}_b$, $\bar{u}_m$.

APPENDIX B: DISTURBANCE EQUATIONS AND BOUNDARY CONDITIONS FOR THE MODAL ANALYSIS

The approach is similar to the one followed by Hill and Straughan [48]. This leads to the constitution of the following eigenvalue problem in the three layers [Eqs. (B1)–(B4) correspond to

the fluid layer, Eqs. (B5)–(B8) correspond to the transition Brinkman layer, while Eqs. (B9)–(B12) refer to the Darcy layer]:

$$i(\alpha\hat{u}+\beta\hat{v})+D\hat{w}=0, \tag{B1}$$

$$i(c-\alpha\bar{u})\hat{u}-\hat{w}D\bar{u}-i\alpha\hat{p}+\frac{1}{\mathrm{Re}}[\bar{\mu}(D^2-\alpha^2-\beta^2)\hat{u}+D\mu_t(D\hat{u}+i\alpha\hat{w})+(\mu_t-\bar{\mu})(D^2\hat{u}+i\alpha D\hat{w})]=0, \tag{B2}$$

$$i(c-\alpha\bar{u})\hat{v}-i\beta\hat{p}+\frac{1}{\mathrm{Re}}[\bar{\mu}(D^2-\alpha^2-\beta^2)\hat{v}+D\bar{\mu}(D\hat{v}+i\beta\hat{w})]=0, \tag{B3}$$

$$i(c-\alpha\bar{u})\hat{w}-D\hat{p}+\frac{1}{\mathrm{Re}}[\bar{\mu}(D^2-\alpha^2-\beta^2)\hat{w}+2D\bar{\mu}D\hat{w}+(\mu_t-\bar{\mu})i\alpha(D\hat{u}+i\alpha\hat{w})]=0, \tag{B4}$$

$$i(\alpha_b\hat{u}_b+\beta_b\hat{v}_b)+D_b\hat{w}_b=0, \tag{B5}$$

$$ic_b\hat{u}_b-\left(\frac{\varepsilon}{\mathrm{Re}_b}\right)\left[i\alpha_b\hat{p}_b+\frac{n}{P_n}\cdot\frac{\bar{u}_b^{n-1}}{\delta^{n+1}}\cdot\hat{u}_b-\frac{1}{\varepsilon^n}\{\Omega\,\hat{u}_b+D_b\mu_{tb}(D_b\hat{u}_b+i\alpha_b\hat{w}_b)+D_b\,\Gamma_b\}\right]=0, \tag{B6}$$

$$ic_b\hat{v}_b-\left(\frac{\varepsilon}{\mathrm{Re}_b}\right)\left[i\beta_b\hat{p}_b+\frac{1}{P_n}\cdot\frac{\bar{u}_b^{n-1}}{\delta^{n+1}}\cdot\hat{v}_b-\frac{1}{\varepsilon^n}\{\Omega\hat{v}_b+D_b\bar{\mu}_b(D_b\hat{v}_b+i\beta_b\hat{w}_b)\}\right]=0, \tag{B7}$$

$$ic_b\hat{w}_b-\left(\frac{\varepsilon}{\mathrm{Re}_b}\right)\left[D_b\hat{p}_b+\frac{1}{P_n}\cdot\frac{\bar{u}_b^{n-1}}{\delta^{n+1}}\cdot\hat{w}_b-\frac{1}{\varepsilon^n}\{\Omega\hat{w}_b+2D_b\bar{\mu}_bD_b\hat{w}_b+i\alpha_b\Gamma_b\}\right]=0, \tag{B8}$$

$$i(\alpha_m\hat{u}_m+\beta_m\hat{v}_m)+D_m\hat{w}_m=0, \tag{B9}$$

$$ic_m\hat{u}_m-\left(\frac{\varepsilon}{\mathrm{Re}_m}\right)\left(i\alpha_m\hat{p}_m+\frac{n}{P_n}\cdot\frac{\bar{u}_m^{n-1}}{\delta^{n+1}}\cdot\hat{u}_m\right)=0, \tag{B10}$$

$$ic_m\hat{v}_m-\left(\frac{\varepsilon}{\mathrm{Re}_m}\right)\left(i\beta_m\hat{p}_m+\frac{1}{P_n}\cdot\frac{\bar{u}_m^{n-1}}{\delta^{n+1}}\cdot\hat{v}_m\right)=0, \tag{B11}$$

$$ic_m\hat{w}_m-\left(\frac{\varepsilon}{\mathrm{Re}_m}\right)\left(D_m\hat{p}_m+\frac{1}{P_n}\cdot\frac{\bar{u}_m^{n-1}}{\delta^{n+1}}\cdot\hat{w}_m\right)=0. \tag{B12}$$

Equations (B1)–(B12) constitute a fifteenth-order problem. To solve the same, the boundary conditions are as follows:

At the upper wall (i.e., $\bar{z}=1$),

$$\hat{u}=0,\quad \hat{v}=0,\quad \hat{w}=0\,. \tag{B13}$$

At the interface of the fluid and the Brinkman layers (i.e., $\bar{z}=0$),

$$\hat{u}=\frac{\hat{d}^{\frac{1}{n}}\mathrm{Re}_b}{\mathrm{Re}}\left[\frac{\left(\frac{n}{n+1}\right)(1-\bar{z}_0)^{\frac{n+1}{n}}}{(P_n\,\delta^{n+1})^{\frac{1}{n}}}\right]^{1-n}\hat{u}_b,\quad \hat{v}=\frac{\hat{d}^{\frac{1}{n}}\mathrm{Re}_b}{\mathrm{Re}}\left[\frac{\left(\frac{n}{n+1}\right)(1-\bar{z}_0)^{\frac{n+1}{n}}}{(P_n\,\delta^{n+1})^{\frac{1}{n}}}\right]^{1-n}\hat{v}_b, \tag{B14}$$

$$\hat{w}=\frac{\hat{d}^{\frac{1}{n}}\mathrm{Re}_b}{\mathrm{Re}}\left[\frac{\left(\frac{n}{n+1}\right)(1-\bar{z}_0)^{\frac{n+1}{n}}}{(P_n\,\delta^{n+1})^{\frac{1}{n}}}\right]^{1-n}\hat{w}_b,\quad D\hat{u}=\frac{\mathrm{Re}_b}{\mathrm{Re}}\left(\frac{\hat{d}^{(n+\frac{1}{n})}}{\varepsilon^n}\right)\left[\frac{P_n\,\delta^{n+1}}{\left(\frac{n}{n+1}\right)^n(1-\bar{z}_0)^{n+1}}\right]D_b\hat{u}_b, \tag{B15}$$

$$D\hat{v}=\frac{\mathrm{Re}_b}{\mathrm{Re}}\left(\frac{\hat{d}^{(n+\frac{1}{n})}}{\varepsilon^n}\right)\left[\frac{P_n\,\delta^{n+1}}{\left(\frac{n}{n+1}\right)^n(1-\bar{z}_0)^{n+1}}\right]D_b\hat{v}_b,$$

$$\hat{p}=D\hat{w}+\left(\frac{\mathrm{Re}_b}{\mathrm{Re}}\right)\left(\frac{\hat{d}^{(n+\frac{1}{n})}}{\varepsilon^n}\right)\left[\hat{p}_b-\frac{P_n\,\delta^{n+1}}{\left(\frac{n}{n+1}\right)^n(1-\bar{z}_0)^{n+1}}D_b\hat{w}_b\right]. \tag{B16}$$

At the interface of the Brinkman and the Darcy layers (i.e., $\bar{z}_m = -\beta_{TL}$),

$$D\hat{u}_b = \frac{\alpha_{BJ}\hat{d}}{P_n^{\frac{1}{n+1}}\delta}\left[\hat{u}_b - \frac{\hat{d}^{\frac{1}{n}}\mathrm{Re}_m}{\mathrm{Re}_b}\hat{u}_m\right], \quad D\hat{v}_b = \frac{\alpha_{BJ}\hat{d}}{P_n^{\frac{1}{n+1}}\delta}\left[\hat{v}_b - \frac{\hat{d}^{\frac{1}{n}}\mathrm{Re}_m}{\mathrm{Re}_b}\hat{v}_m\right], \tag{B17}$$

$$\hat{p}_b = \frac{\mathrm{Re}_m}{\mathrm{Re}_b}\left[\left(\frac{\hat{d}^{(n+\frac{1}{n})}}{\varepsilon^n}\right)\hat{p}_m + P_n^2\,\delta^{2(n+1)}D_b\hat{w}_b\right], \quad \hat{w}_b = \frac{\hat{d}^{\frac{1}{n}}\mathrm{Re}_m}{\mathrm{Re}_b}\,\hat{w}_m. \tag{B18}$$

Finally, at the bottom of the porous layer (i.e., $\bar{z}_m = -1$), the conditions are

$$\hat{v}_m = 0, \quad \hat{w}_m = 0. \tag{B19}$$

[1] B. Goyeau, D. Lhuillier, D. Gobin, and M. G. Velarde, Momentum transport at a fluid-porous interface, Int. J. Heat Mass Transfer **46**, 4071 (2003).

[2] A. Goharzadeh, A. Khalili, and B. B. Jorgensen, Transition layer thickness at a fluid-porous interface, Phys. Fluids **17**, 057102 (2005).

[3] M. B. Allen, A. Behie, and J. A. Trangenstein, *Multiphase Flow in Porous Media: Mechanics, Mathematics, and Numerics* (Springer, 1988).

[4] B. Chen, A. Cunningham, R. Ewing, R. Peralta, and E. Visser, Two-dimensional modeling of microscale transport and biotransformation in porous media, Numer. Methods Partial Differ. Equ. **10**, 65 (1994).

[5] R. E. Ewing and S. Weekes, Numerical methods for contaminant transport in porous media, Comput. Math. **202**, 75 (1998).

[6] B. J. Suchomel, B. M. Chen, and M. B. Allen, Network model of flow, transport and biofilm effects in porous media, Transp. Porous Media **30**, 1 (1998).

[7] H. Darcy, *Les Fontaines Publiques de la Ville de Dijon* (Dalmont, Paris, 1856).

[8] D. Jamet, M. Chandesris, and B. Goyeau, On the equivalence of the discontinuous one- and two-domain approaches for the modelling of transport phenomena at a fluid/porous interface, Transp. Porous Media **78**, 403 (2009).

[9] K. Vafai and C. L. Tien, Boundary and inertia effects on flow and heat transfer in porous media, Int. J. Heat Mass Transfer **24**, 195 (1981).

[10] S. Whitaker, *The Method of Volume Averaging* (Springer, Netherlands, 1999).

[11] D. B. Das, V. Nassehi, and R. J. Wakeman, A finite volume model for the hydrodynamics of combined free and porous flow in sub-surface regions, Adv. Environ. Res. **7**, 35 (2002).

[12] N. S. Hanspal, A. N. Waghode, V. Nassehi, and R. J. Wakeman, Numerical analysis of coupled Stokes/Darcy flows in industrial filtrations, Transp. Porous Media **64**, 73 (2006).

[13] C.-H. Bruneau and I. Mortazavi, Passive control of the flow around a square cylinder using porous media, Int. J. Numer. Methods Fluids **46**, 415 (2004).

[14] C.-H. Bruneau and I. Mortazavi, Numerical modelling and passive flow control using porous media, Comput. Fluids **37**, 488 (2008).

[15] T. J. Sadowski, Non-Newtonian flow through porous media. II. Experimental, Trans. Soc. Rheol. **9**, 251 (1965).

[16] T. J. Sadowski and R. B. Bird, Non-Newtonian flow through porous media. I. Theoretical, Trans. Soc. Rheol. **9**, 243 (1965).

[17] A. V. Shenoy, Non-Newtonian fluid heat transfer in porous media, Adv. Heat Transfer **24**, 101 (1994).

[18] N. B. Khelifa, Z. Alloui, H. Beji, and P. Vasseur, Natural convection in a horizontal porous cavity filled with a non-Newtonian binary fluid of power-law type, J. Non-Newtonian Fluid Mech. **169-170**, 15 (2012).

[19] C. Chahtour, H. B. Hamed, H. Beji, A. Guizani, and W. Alimi, Convective hydromagnetic instabilities of a power-law liquid saturating a porous medium: Flux conditions, Phys. Fluids **30**, 013101 (2018).

[20] D. A. Nield and A. Bejan, *Convection in Porous Media*, 3rd ed. (Springer, New York, 2006).
[21] D. A. Nield, The boundary correction for the Rayleigh-Darcy problem: Limitations of the Brinkman equation, J. Fluid Mech. **128**, 37 (1983).
[22] D. A. Nield, The limitations of the Brinkman-Forchheimer equation in modeling flow in a saturated porous medium and at an interface, Int. J. Heat Fluid Flow **12**, 269 (1991).
[23] D. A. Nield, Modelling the effect of surface tension on the onset of natural convection in a saturated porous medium, Transp. Porous Media **31**, 365 (1998).
[24] J. W. Lu and F. Chen, Assessment of mathematical models for the flow in directional solidification, J. Crystal Growth **171**, 601 (1997).
[25] M. H. Chang, F. Chen, and B. Straughan, Instability of Poiseuille flow in a fluid overlying a porous layer, J. Fluid Mech. **564**, 287 (2006).
[26] P. Deepu, S. Dawande, and S. Basu, Instabilities in a fluid overlying an inclined anisotropic and inhomogeneous porous layer, J. Fluid Mech. **762**, R2 (2015).
[27] P. Deepu, P. Anand, and S. Basu, Stability of Poiseuille flow in a fluid overlying an anisotropic and inhomogeneous porous layer, Phys. Rev. E **92**, 023009 (2015).
[28] P. Deepu, S. Kallurkar, P. Anand, and S. Basu, Stability of a liquid film flowing down an inclined anisotropic and inhomogeneous porous layer: An analytical description, J. Fluid Mech. **807**, 135 (2016).
[29] T. Y. Chang, F. Chen, and M. H. Chang, Stability of plane Poiseuille-Couette flow in a fluid layer overlying a porous layer, J. Fluid Mech. **826**, 376 (2017).
[30] A. Samanta, Role of slip on the linear stability of a liquid flow through a porous channel, Phys. Fluids **29**, 094103 (2017).
[31] S. Sengupta and S. De, Stability of Poiseuille flow of a Bingham fluid overlying an anisotropic and inhomogeneous porous layer, J. Fluid Mech. **874**, 573 (2019).
[32] S. Sengupta and S. De, Effect of Couette component on the stability of Poiseuille flow of a Bingham fluid-porous system: Modal and non-modal approaches, Phys. Fluids **32**, 064103 (2020).
[33] L. Durlofsky and J. F. Brady, Analysis of the Brinkman equation as a model for flow in porous media, Phys. Fluids **30**, 3329 (1987).
[34] J. L. Auriault, On the domain of validity of Brinkman's equation, Trans. Porous Media **79**, 215 (2009).
[35] A. A. Hill and B. Straughan, Poiseuille flow in a fluid overlying a highly porous material, Adv. Water Resour. **32**, 1609 (2009).
[36] R. Liu, Q. S. Liu, and S. C. Zhao, Instability of plane Poiseuille flow in a fluid-porous system, Phys. Fluids **20**, 104105 (2008).
[37] Z. Wu and P. Mirbod, Instability analysis of the flow between two parallel plates where the bottom one coated with porous media, Adv. Water Resour. **130**, 221 (2019).
[38] C. Y. Choi and P. M. Waller, Momentum transport mechanism for water flow over porous media, J. Environ. Eng. **123**, 792 (1997).
[39] S. K. Gupte and S. G. Advani, Flow near the permeable boundary of porous medium: An experimental investigation using LDA, Exp. Fluids **22**, 408 (1997).
[40] A. Goharzadeh, A. Saidi, D. Wang, W. Merzkirch, and A. Khalili, An experimental investigation of the Brinkman layer thickness at a fluid-porous interface, in *One Hundred Years of Boundary Layer Research*, edited by G. E. A. Meier and K. R. Sreenivasan (Springer, New York, 2006), pp. 445–454.

[41] M. Parvazinia, V. Nassehi, R. J. Wakeman, and M. H. R. Ghoreishy, Finite element modelling of flow through a porous medium between two parallel plates using the Brinkman equation, Transp. Porous Media **63**, 71 (2006).
[42] M. Chandesris and D. Jamet, Jump conditions and surface-excess quantities at a fluid-porous interface: A multi-scale approach, Transp. Porous Media **78**, 419 (2009).
[43] M. R. Morad and A. Khalili, Transition layer thickness in a fluid-porous medium of multi-sized spherical beads, Exp. Fluids **46**, 323 (2009).
[44] D. A. Nield and A. V. Kuznetsov, The effect of a transition layer between a fluid and a porous medium: Shear flow in a channel, Transp. Porous Media **78**, 477 (2009).
[45] K. Tao, J. Yao, and Z. Huang, Analysis of the laminar flow in a transition layer with variable permeability between a free-fluid and a porous medium, Acta Mech. **224**, 1943 (2013).
[46] R. Usha and S. Naire, A thin film on a porous substrate: A two-sided model, dynamics and stability, Chem. Eng. Sci. **89**, 72 (2013).
[47] M. Kaviany, *Principles of Heat Transfer in Porous Media* (Springer, New York, 1995).
[48] A. A. Hill and B. Straughan, Poiseuille flow in a fluid overlying a porous medium, J. Fluid Mech. **603**, 137 (2008).
[49] A. A. Hill, Instability of Poiseuille flow in a fluid overlying a glass bead packed porous layer, Acta Mech. **206**, 95 (2009).
[50] J. Jiménez, M. Uhlmann, A. Pinelli, and G. Kawahara, Turbulent shear flow over active and passive porous surfaces, J. Fluid Mech. **442**, 89 (2001).
[51] R. H. Christopher and S. Middleman, Power-law flow through a packed tube, Ind. Eng. Chem. Fundam. **4**, 422 (1965).
[52] Z. Kemblowski and M. Michniewicz, A new look at the laminar flow of power-law fluids through granular beds, Rheol. Acta **18**, 730 (1979).
[53] R. V. Dharmadhikari and D. D. Kale, Flow of non-Newtonian fluids through porous media, Chem. Eng. Sci. **40**, 527 (1985).
[54] G. S. Beavers and D. D. Joseph, Boundary conditions at a naturally permeable wall, J. Fluid Mech. **30**, 197 (1967).
[55] A. R. Rao and M. Mishra, Peristaltic transport of a power-law fluid in a porous tube, J. Non-Newtonian Fluid Mech. **121**, 163 (2004).
[56] J. P. Pascal, Instability of power-law fluid down a porous incline, J. Non-Newtonian Fluid Mech. **133**, 109 (2006).
[57] C. Nouar, A. Bottaro, and J. P. Brancher, Delaying transition to turbulence in channel flow: Revisiting the stability of shear-thinning fluids, J. Fluid Mech. **592**, 177 (2007).
[58] R. Liu and Q. S. Liu, Non-modal instability in plane Couette flow of a power-law fluid, J. Fluid Mech. **676**, 145 (2011).
[59] P. J. Schmid and D. S. Henningson, *Stability and Transition in Shear Flows* (Springer, New York, 2001).
[60] S. C. Reddy and D. S. Henningson, Energy growth in viscous channel flows, J. Fluid Mech. **252**, 209 (1993).
[61] T. Herbert, Secondary instability of boundary layers, Ann. Rev. Fluid Mech. **20**, 487 (1988).
[62] G. Iuso, G. M. Di Cicca, M. Onorato, P. G. Spazzini, and R. Malvano, Velocity streak structure modifications induced by flow manipulation, Phys. Fluids **15**, 2602 (2003).
[63] J. A. Ochoa-Tapia and S. Whitaker, Momentum transfer at the boundary between a porous medium and a homogeneous fluid—I. Theoretical development, Int. J. Heat Mass Transfer **38**, 2635 (1995).
[64] P. G. Drazin and W. H. Reid, *Hydrodynamic Stability*, 2nd ed. (Cambridge University Press, 2004).
[65] B. Straughan, *Stability and Wave Motion in Porous Media* (Springer, New York, 2008).